

Variable Faint Optical Sources Discovered by Comparing POSS and SDSS Catalogs

Branimir Sesar^{1,2}, Domjan Svilković¹, Željko Ivezić^{2,3}, Robert H. Lupton², Jeffrey A. Munn⁴, Douglas Finkbeiner^{2,5}, William Steinhardt², Rob Siverd², David E. Johnston², Gillian R. Knapp², James E. Gunn², Constance M. Rockosi⁶, David Schlegel², Daniel E. Vanden Berk⁷, Pat Hall^{2,8}, Donald P. Schneider⁹, Robert J. Brunner¹⁰

ABSTRACT

We present a study of variable faint optical sources discovered by comparing the Sloan Digital Sky Survey (SDSS) and the Palomar Observatory Sky Survey (POSS) catalogs. We use SDSS measurements to photometrically recalibrate several publicly available POSS catalogs (USNO-A2.0, USNO-B1.0, GSC2.2 and DPOSS). A piecewise recalibration of the POSS data in 100 arcmin² patches (one SDSS field) generally results in an improvement of photometric accuracy (rms) by nearly a factor of two, compared to the original data. In addition to the smaller core width of the error distribution, the tails of the distribution become much steeper after the recalibration. These improvements are mostly due to the very dense grid of calibration stars provided by SDSS, which rectifies the intrinsic inhomogeneities of Schmidt plates. We find that the POSS I magnitudes can be improved to ~ 0.15 mag accuracy, and POSS II magnitudes

¹University of Zagreb, Dept. of Physics, Bijenička cesta 32, 10000 Zagreb, Croatia

²Princeton University Observatory, Princeton, NJ 08544

³H.N. Russell Fellow, on leave from the University of Washington

⁴U.S. Naval Observatory, Flagstaff Station, P.O. Box 1149, Flagstaff, AZ 86002

⁵Hubble Fellow

⁶University of Washington, Dept. of Astronomy, Box 351580, Seattle, WA 98195

⁷University of Pittsburgh, Dept. of Physics & Astronomy, 3941 O'Hara Street, Pittsburgh, PA 15260

⁸Pontificia Universidad Católica de Chile, Departamento de Astronomía y Astrofísica, Facultad de Física, Casilla 306, Santiago 22, Chile

⁹Department of Astronomy and Astrophysics, The Pennsylvania State University, University Park, PA 16802

¹⁰NCSA and Department of Astronomy, University of Illinois, Urbana, IL 61801

to ~ 0.10 mag accuracy. The smallest final errors are obtained with the GSC2.2 catalog for which they approach 0.07 mag at the bright end.

We use the recalibrated catalogs for the $\sim 2,000$ deg² of sky in the SDSS Data Release 1 to construct a catalog of $\sim 60,000$ sources variable on time scales 10-50 years. We find that at least 1% of faint optical sources appear variable at the >0.2 mag level, and that about 10% of the variable population are quasars, although they represent only 0.25% of all point sources in the adopted flux-limited sample. A series of statistical tests based on the morphology of SDSS color-magnitude and color-color diagrams, as well as visual comparison of images and comparison with repeated SDSS observations, demonstrate the robustness of the selection methods. Candidate variable sources are correctly identified in more than 95% of cases, and the fraction of true variables among the selected candidates is as high as 73%. We quantify the distribution of variable sources in the SDSS color-color diagrams, and the variability characteristics of quasars. The observed long-term variability (structure function) is smaller than predicted by the extrapolation of the power-law measured for short time scales using repeated SDSS imaging (0.35 vs. 0.60 mag for SDSS-POSS I, and 0.24 vs. 0.35 mag for SDSS-POSS II, rms). This turn-over in structure function suggests that the characteristic time scale for quasar variability is of the order one year. The long-term ($\gtrsim 1$ year) quasar variability decreases with luminosity and rest-frame wavelength similarly to the short-term ($\lesssim 1$ year) behavior. We also demonstrate that candidate RR Lyrae stars trace the same halo structures, such as the Sgr dwarf tidal stream, that were discovered using repeated SDSS observations. We utilize the POSS-SDSS selected candidates to constrain the halo structure in the parts of sky for which repeated SDSS observations do not exist.

Subject headings: Galaxy: halo — Galaxy: stellar content — variables: RR Lyrae variable — quasars: variability

1. Introduction

The time domain represents another dimension, in addition to spectral and spatial, in the exploration of celestial objects. Despite the importance of variability phenomena, the properties of optically faint variable sources are by and large unknown. There are about 10^9 stars brighter than $V = 20$ in the sky, and at least 3% of them are expected to be variable

at a few percent level (Eyer, 1999). However, the overwhelming majority are not recognized as variables even at the brightest magnitudes: 90% of variable stars with $V < 12$ remain to be discovered (Paczynski, 2000). Paczynski (1996) lists striking examples of the serious incompleteness in the available samples of variable stars: eclipsing binaries of Algol type, and contact binaries (W UMa stars) are incomplete fainter than $V \sim 12$, and RS CVn type binaries are complete only to $V \sim 5$. Another vivid example of serious selection effects is the sky distribution of RR Lyrae stars: objects listed in the 4th General Catalogue of Variable Stars (the main resource for variable stars) are distributed in isolated square patches with the size and shape of the Schmidt plates used to discover them.

The discrepancy between the utility of variable stars and the available observational data has prompted several contemporary projects aimed at regular monitoring of the optical sky. The current state-of-the-art also greatly benefited from past and present microlensing searches (Paczynski, 2001). Some of the more prominent surveys in terms of the sky coverage, depth, and cadence are:

- The Faint Sky Variability Survey (Huber, Howell, Everett & Groot, 2002) is a very deep ($V < 24$) *BVI* survey of 23 deg² of sky, containing about 80,000 sources
- The QUEST Survey (Vivas et al. 2001) monitors 600 deg² of sky to a limit of $V = 21$.
- ROTSE (Akerlof et al. 2003) monitors the entire observable sky twice a night to a limit of $V = 15.5$.
- OGLE (most recently OGLE III; Udalski et al. 2002) monitors ~ 100 deg² towards the Galactic bulge to a limit of $I = 20$. Due to a very high stellar density towards the bulge, OGLE II has detected over 200,000 variable stars (Woźniak et al. 2002).

These and other surveys have demonstrated that in addition to variable stars, there are many other exciting photometrically variable objects in the sky. For example, ROTSE I detected an optical flash generated by a gamma ray burst at a redshift of 1.6, the most luminous optical source ever measured ($V = 9$, $M_V = -36.4$, Vestrand et al. 2002). The detection of such optical flashes may place strong constraints on the physical mechanisms responsible for gamma ray bursts. Similarly, the variability of quasars offers significant clues for the origin of their emission (e.g. Trevese, Kron & Bunone, 2001).

Recognizing the outstanding importance of variable objects, the last Decadal Survey Report highly recommended a major new initiative for studying the variable sky, the Large

Synoptic Survey Telescope (LSST). The LSST¹¹ will offer an unprecedented view of the faint variable sky: according to the current designs it will scan the entire accessible sky every three nights to a limit of $V \sim 24$. Compared to any other survey currently available, the data from LSST will be revolutionary. Yet, at least half a decade or more will elapse before the first photons are detected by the LSST. Meanwhile, the already available Palomar Digital Sky Surveys (POSS I and POSS II, for references see Appendix A) and ongoing Sloan Digital Sky Survey (see Section 2.2) can be used to study the properties of faint ($r \sim 20$) optical sources, and here we present such a study.

The comparison of the POSS and SDSS surveys allows studies of the long term variability with time scales of up to half a century. By necessity, such studies are based on a small number of observations of the same objects to constrain the ensemble properties of a sample of sources, as opposed to studying well-sampled light curves for a small number of objects. The lack of detailed information for individual objects is compensated in some ways by the large sample size. In addition, the 5-band accurate SDSS photometry can be used for very detailed source classification; e.g. separation of quasars and stars (Richards et al. 2002), spectral classification of stars to within 1-2 spectral subtypes (Lenz et al. 1998, Finlator et al. 2000, Hawley et al. 2002), and even remarkably efficient color selection (thanks to accurate u band photometry) of the low-metallicity G and K giants (Helmi et al. 2002) and horizontal branch stars (Yanny et al. 2000, Ivezić 2003a).

However, when using only a few epochs of observations, the robustness of variability detection critically depends on the stability of the photometric errors. While the SDSS photometric errors are small (~ 0.02) and well behaved (Ivezić et al. 2003b), older photographic POSS data can have large errors (tenths of mag) due to intrinsic inhomogeneities of Schmidt plates and the lack of a sufficient number of calibration stars. This problem can be alleviated to some extent by using photometric measurements of stars in the SDSS to recalibrate POSS catalogs. In Section 2 we describe such a recalibration method and demonstrate that photometric errors in the POSS catalogs can be decreased by a factor of ~ 2 (rms), with a significant improvement in the behavior of the error distribution tails. In Section 3, we use SDSS data and recalibrated POSS catalogs to select variable objects in $\sim 2000 \text{ deg}^2$ of sky from the SDSS Data Release 1 (Abazajian et al. 2003). In the same section we discuss tests which demonstrate the robustness of the selection algorithm, and quantify the distribution of variable sources in the SDSS color-color diagrams. The Milky Way halo structure traced by selected candidate RR Lyrae stars is discussed in Section 4, and in Section 5 we analyze the variability of quasars. Our main results are

¹¹There are currently two designs considered for implementation: a distributed aperture approach (Pan-STARRS, Kaiser et al. 2002) and a single large-aperture telescope (Tyson 2002).

summarized in Section 6.

2. The Photometric Recalibration of POSS Catalogs using SDSS Measurements

2.1. The Input POSS Catalogs

We utilize several publicly available POSS catalogs: USNO-A2.0, USNO-B1.0, GSC2.2 and DPOSS. A description of each catalog and references are listed in Appendix A. Here we briefly mention that all four catalogs utilize the same POSS I and POSS II Schmidt plates. However, the scanning and calibration procedures are different, and the source parameters, such as magnitudes, reported in different catalogs in general are not the same for the same sources detected on the same plates. USNO-A2.0 reports O and E magnitudes, hereafter O_a and E_a to distinguish them from O and E magnitudes reported in the USNO-B1.0 catalog. The latter catalog also lists J , F and N magnitudes. The GSC2.2 catalog lists J and F magnitudes, hereafter J_g and F_g to distinguish them from J and F magnitudes reported in the USNO-B1.0 catalog. The DPOSS catalog is also based on photographic J , F and N , but they are calibrated and reported as G , R and I magnitudes.

The completeness of the USNO-B1.0 catalog, measured using SDSS data, is discussed by Munn et al. (2004). Our analysis of other catalogs confirms their result that, in general, POSS catalogs are $\sim 95\%$ complete at magnitudes brighter than 19–20 (depending on a particular band/catalog), and have faint limits (which we define as the magnitude where fewer than 50% of SDSS sources are found in a POSS catalog) at $m \sim 20.5 - 21$.

2.2. Sloan Digital Sky Survey

The SDSS is a digital photometric and spectroscopic survey which will cover up to one quarter of the Celestial Sphere in the North Galactic cap, and produce a smaller area ($\sim 225 \text{ deg}^2$) but much deeper survey in the Southern Galactic hemisphere¹² (York et al. 2000, Stoughton et al. 2002, Abazajian et al. 2003). The flux densities of detected objects are measured almost simultaneously in five bands (u , g , r , i , and z) with effective wavelengths of 3540 Å, 4760 Å, 6280 Å, 7690 Å, and 9250 Å (Fukugita et al. 1996, Gunn et al. 1998, Smith et al. 2002, Hogg et al. 2002). The completeness of SDSS catalogs for point sources

¹²See also <http://www.astro.princeton.edu/PBOOK/welcome.htm>

is $\sim 99.3\%$ at the bright end (Ivezić et al. 2001), and drops to 95% at limiting magnitudes¹³ of 22.1, 22.4, 22.1, 21.2, and 20.3 (the SDSS saturation limit is ~ 14 in the r band, and somewhat brighter in other bands). All magnitudes are given on the AB_v system (Oke & Gunn 1983, for additional discussion regarding the SDSS photometric system see Fukugita et al. 1996 and Fan 1999). The survey sky coverage of about π steradians (10,000 deg²) will result in photometric measurements to the above detection limits for about 100 million stars and a similar number of galaxies. Astrometric positions are accurate to about 0.1 arcsec per coordinate for sources brighter than $r \sim 20.5^m$ (Pier et al. 2003), and the morphological information from the images allows robust star-galaxy separation to $r \sim 21.5^m$ (Lupton et al. 2003). More technical details may be found in Stoughton et al. (2002), and on the SDSS web site (<http://www.sdss.org>).

In this work we use the SDSS Data Release 1, which provides data for 2099 deg² of the sky. The equatorial Aitoff projection of this area can be found at the SDSS web site (also Fig. 5 in Ivezić et al. 2003a).

2.3. Photometric Transformations Between POSS and SDSS Systems

We chose to synthesize magnitudes in the POSS bands using SDSS measurements, and then recalibrate POSS catalogs using their original bands. The alternative of recalibrating POSS catalogs directly to the SDSS system is less desirable because colors at the POSS epoch are poorly known, and this may have an effect on the photometric accuracy for variable sources. Following Monet et al. (2003), we adopt the following form to define synthetic POSS magnitudes, m_{SDSS} , calculated from SDSS photometry:

$$m_{SDSS} = m + b \text{ color} + c \tag{1}$$

where $m = g, r, g, r, i$ and $\text{color} = g - r, g - r, g - r, g - r, r - i$ for $O, E, J, F,$ and N , respectively (e.g. $O_{SDSS} = g + b(g - r) + c$). Utilizing data for about ~ 300 deg² of sky (SDSS runs 752 and 756), we derived the best-fit values of coefficients b and c for each band and the POSS catalog. We used only “good” sources defined as:

1. Sources must be unresolved in SDSS data (note that the SDSS star-galaxy separation is robust to at least $r^* \sim 21.5$, which is significantly fainter than the faint limit of the resulting sample).

¹³These values are determined by comparing multiple scans of the same area obtained during the commissioning year. Typical seeing in these observations was 1.5 ± 0.1 arcsec.

2. Sources must be isolated in SDSS data. This condition ensures that the USNO/GSC/DPOSS photometry is not affected by difficult to measure, blended objects
3. Sources must not be saturated in g or r band in the SDSS data (roughly equivalent to $g, r > 14^m$), and must have $g < 19$.
4. The USNO/GSC/DPOSS and SDSS positions must agree to better than $2''$. This limit corresponds to a $\sim 5\sigma$ cut on astrometric errors (Pier et al. 2003).
5. The sources must have $u - g > 0.7$ (measured by SDSS) to avoid highly variable quasars (see Section 5).

The best-fit values of coefficients b and c , and the residual rms scatter (which is a good measure of the mean photometric accuracy of the POSS catalogs) are listed in Table 1. Note that J and F magnitudes from the GSC2.2 catalog have the smallest residual scatter, while the O and E magnitudes have the largest scatter.

Similar values for b and c coefficients were derived for the USNO-B1.0 magnitudes by Monet et al. (2003). We have verified that adopting their transformations results in only slightly larger residual scatter for the other three catalogs. Thus, in order to prevent proliferation of various SDSS-POSS transformations, we adopt their transformations, which we list below for completeness, in the rest of this work (for DPOSS G and R magnitudes¹⁴, we use coefficients listed in Table 1).

$$\begin{aligned}
 O_{\text{SDSS}} &= g + 0.452(g - r) + 0.08 \\
 E_{\text{SDSS}} &= r - 0.086(g - r) - 0.20 \\
 J_{\text{SDSS}} &= g + 0.079(g - r) + 0.06 \\
 F_{\text{SDSS}} &= r - 0.109(g - r) - 0.09 \\
 N_{\text{SDSS}} &= i - 0.164(r - i) - 0.44
 \end{aligned}
 \tag{2}$$

¹⁴We use upper case letters for DPOSS magnitudes to distinguish them from SDSS g and r magnitudes.

2.4. The Recalibration Method

The first basic premise of the recalibration method employed here is that the SDSS photometric errors are negligible compared to errors in the POSS catalogs – the SDSS photometric errors are ~ 0.02 mag, as demonstrated by repeated scans (Ivezić et al. 2003b), while the errors in the POSS catalogs are 0.1 mag or larger. The second premise is that not more than a few percent of faint stars vary by more than a few percent, in agreement with the available data and models (Eyer 1999). The third assumption is that systematic errors are a significant contribution to photometric errors in the POSS catalog, and thus can be calibrated out using a dense grid of calibration stars provided by SDSS. We demonstrate empirically that indeed the accuracy of POSS-based photometry can be improved by about a factor of 2 in all analyzed catalogs.

The recalibration of the POSS catalogs is performed in two steps. In the first step the subsamples of “good” objects (see Section 2.3) are grouped by Schmidt plate and SDSS fields. One SDSS field has an area of 0.034 deg^2 ; this is sufficiently large to include enough calibration stars (typically 50-200), and yet sufficiently small that the response of the Schmidt plates is nearly constant, as shown by Lattanzi & Bucciarelli (1991). To avoid edge effects, we use a running window with the width of 3 SDSS fields (0.45° , see the next section for more details).

For each of the five POSS magnitudes, we minimize $\sum(m_{recalib} - m_{SDSS})^2$ using the least-square method, where

$$m_{recalib} = A * m_{POSS} + B * color + C, \quad (3)$$

and $m = O, E, J, F, N$ (m_{SDSS} are defined by eq. 2). This step removes systematic magnitude errors due to local non-linearities of the plate, color-term dependence and zero-point offsets¹⁵. In the second step, we use all the “good” sources from a given Schmidt plate ($\sim 36 \text{ deg}^2$) to correct the dependence of the $m_{recalib} - m_{SDSS}$ residuals on magnitude (using median $m_{recalib} - m_{SDSS}$ in 1 mag wide bins, and linear interpolation between the bin centers). Such residuals are typically larger at the faint end, and are probably caused by incorrect sky estimates in the POSS catalogs.

¹⁵A similar procedure was used by Munn et al. (2004) for astrometric recalibration of POSS catalogs.

2.4.1. *The Optimal Recalibration Scale*

As advocated by Lattanzi & Bucciarelli (1991), the characteristic scale for inhomogeneities in Schmidt plates is about 0.5° . We tested their result by recalibrating POSS-II *J* band plates by varying the calibration window width. Fig. 1 shows the final errors as a function of that width for three plates. As expected, the decrease of calibration window width decreases photometric errors all the way to practical limit of $\sim 0.5^\circ$ set by the minimum number of required calibration stars. The figure demonstrates that improvement in accuracy by decreasing the window width from ~ 0.5 - 1° to 0 is only ~ 0.01 mag, thus confirming the result of Lattanzi & Bucciarelli. Note that when extrapolating curves to zero window width, plates show varying photometric accuracy, reflecting different intrinsic properties.

The plate-dependent systematic photometric errors in POSS catalogs are illustrated in Figs. 2–4 (the behavior for USNO-B1.0 catalog is similar). The large jumps in photometric errors at the boundaries of 6 degree wide Schmidt plates are obvious, and suggest that the photometric recalibration of POSS data is mandatory when searching for variable sources that vary less than a few tenths of a magnitude.

2.5. Analysis of the Recalibration Results

2.5.1. *Recalibration Results for the USNO Catalogs*

The results of two recalibration steps, described in the previous section, are illustrated for the USNO-A2.0 catalog in Fig. 5. As evident from the middle panels, the first step results in smaller scatter between SDSS and recalibrated POSS magnitudes, but the magnitude dependence of their differences remains appreciable. This dependence is removed in the second recalibration step, as discernible from the bottom panels.

The recalibration procedure generally results in about a factor of 2 improvement in the root-mean-square (rms) scatter between SDSS-based synthetic POSS magnitudes and the measured POSS magnitudes. Fig. 6 compares the POSS-SDSS magnitude differences before (thin lines) and after (thick lines) calibration, for *O* and *E* bands, on a linear and logarithmic scale. As evident, the recalibration not only results in a smaller rms scatter, but also significantly clips the tails. Both effects are of crucial importance when selecting variable objects.

The corresponding results for the USNO-B1.0 catalog are shown in Figs. 7 and 8. We note that the original *O* and *E* magnitudes have somewhat smaller errors in the USNO-A2.0

catalog, but the USNO-B1.0 magnitudes are marginally better after recalibration.

2.5.2. *Recalibration Results for the GSC2.2 and DPOSS Catalogs*

The main difference between the recalibration of GSC2.2 and other catalogs is the lack of plate information¹⁶ which prevented the second recalibration step. Nevertheless, Figs. 9 and 10 show that for the GSC2.2 catalog the magnitude dependence of the differences between SDSS and recalibrated POSS magnitudes is minor. The results for the DPOSS catalog are shown in Figs. 11 and 12.

2.5.3. *Summary of Recalibration Results*

A summary comparison of the original and recalibrated magnitudes is shown in Fig.13. The rms values of magnitude differences before and after the recalibration for all the catalogs and bands are listed in Table 2. The final errors for the POSS II magnitudes are generally smaller (~ 0.10 mag) than for the POSS I magnitudes (~ 0.15 mag), both evaluated for stars brighter than $g = 19$. The smallest final errors are obtained with the GSC2.2 catalog for which they approach 0.07 mag at the bright end.

3. **Preliminary Analysis of the POSS-SDSS Catalogs of Variable Sources**

The comparison of the SDSS photometric catalog with photometrically recalibrated POSS catalogs can yield a large number of variable sources. Various methods can be employed to produce such a list of candidate variables, depending on whether each band/catalog is considered separately or not, on the cutoff values for magnitude differences, the sample faint limit, etc. The DPOSS catalog is the main catalog used in the subsequent analysis (while the smallest final errors are produced with the GSC2.2 catalog, its public version is not as deep as the DPOSS catalog). For the POSS I survey we chose the USNO-A2.0 catalog (the other option is USNO-B1.0; the photometric errors after recalibration are similar for both USNO catalogs) because it is distributed as a part of the SDSS Data Release 1 (Abazajian et al. 2003).

¹⁶Observations listed in the catalog are collected from multiple plates, even if confined to a small sky region, and the plate number from which a particular entry was derived is not provided.

The criteria for selecting candidate variable sources are described in the next section, and a series of tests for estimating the selection reliability are described in the subsequent section.

3.1. Selection Criteria

When selecting candidate variable sources we consider each POSS band individually for two reasons. First, sometimes POSS observations of the same sky regions were not obtained at the same time, and treating each epoch separately increases the selection completeness for sources variable on short time scales. Second, additional constraints that combine different bands (e.g. “a source must vary in both *O* and *E* band”) can be easily imposed after the initial single-band based selection. We consider only isolated point sources detected by both POSS and SDSS. An initial attempt to isolate orphaned sources detected by only one survey was impeded by the large number of false positives due to problems with POSS plates, and is postponed for future analysis.

For each catalog and band we define the faint magnitude limit, m_{faint} , minimum flux variation, $\Delta m = |m_{SDSS} - m_{POSS}|$, and its minimum significance, $\chi = \Delta m / \sigma$. For the photometric error, σ , we take the rms scatter for all the stars in a given calibration patch and in 0.5 mag wide magnitude bins (using a linear interpolation of binned errors as a function of magnitude). The adopted values of selection parameters for each catalog are listed in Table 3, as well as the number of selected candidate variable sources. In general, the Δm condition controls the selection at the bright end, while the χ condition limits the sample at the faint end. Thus, the selection efficiency is roughly independent of magnitude until about 1-1.5 mag above the adopted faint limit, m_{faint} , when it starts decreasing. We find that typically 15-20% of selected candidates simultaneously satisfy conditions in two bands from a given catalog.

These particular selection criteria were adopted after a trial and error procedure which utilized tests described in the next section. We chose to err on the conservative side and increase catalog robustness at the expense of its completeness, since the small number of epochs already introduced substantial incompleteness. Hence, the fraction of variable sources reported here is only a lower limit.

3.2. Tests of the Selection Reliability

Given the selection criteria described in the previous section, it is necessary for subsequent analysis to estimate the completeness and efficiency of the resulting samples. The selection completeness, the fraction of true variable sources in the analyzed sky region and observed magnitude range selected by the algorithm, is certainly low because the selection is based on variations in only one bandpass, and a fairly large Δm cutoff compared to the typical amplitudes of variable sources (e.g. most RR Lyrae stars and quasars have peak-to-peak amplitudes $\lesssim 1$ mag). For example, Ivezić et al. (2000) used two-epoch SDSS measurements to select candidate RR Lyrae stars and obtained completeness of $\sim 50\%$ for a Δm cutoff of 0.15 mag. With larger Δm cutoffs adopted here, the expected selection completeness for RR Lyrae stars is about 20% (see Section 4 for a direct measurement). The completeness for other types of variable source depends on the shape and amplitudes of their light curves and is hard to estimate, but for most sources is similarly low. While such a low completeness cannot be avoided with the available data, its stability across the sky can be controlled. Such a stability is demonstrated by the lack of features in the distribution of quasars selected by variability, as well as by the recovery of known structures in the distribution of RR Lyrae stars, as discussed below.

The selection efficiency, the fraction of true variable sources in the selected sample, may severely impact the analysis if not sufficiently large. We demonstrate using a series of tests that the selection efficiency is indeed very large (73%) and thus allows a robust analysis of variable faint optical sources.

The main diagnostic for the robustness of the adopted selection criteria is the distribution of selected candidates in SDSS color-magnitude and color-color space. Were the selection a random process, the selected candidates would have the same distribution as the whole sample. However, we find that the samples of candidate variables have a significantly different distribution, as detailed below. The most robust and quantitative test for estimating selection reliability is a comparison with repeated SDSS imaging observations, though applicable to only a small fraction ($\sim 10\%$) of the sky area discussed here where such SDSS observations exist. Another powerful test for candidates with large suspected flux variation ($\gtrsim 0.5$ mag) is a simple visual comparison of POSS and SDSS images. While we found a number of spurious candidates using this method, their fraction is not large enough to significantly affect our results.

3.2.1. *The Distribution of Candidate Variable Sources in SDSS Color-color Diagrams*

The position of a source in SDSS color-magnitude and color-color diagrams is a good proxy for its classification. The distribution of selected candidate variables with $g < 19$ (using the DPOSS catalog, and restrictive selection criteria, entries 7 and 8 from Table 3) in representative diagrams is shown in Fig. 14 (the measured magnitudes are corrected for interstellar extinction using the map from Schlegel, Finkbeiner & Davis 1998). The top row is shown for reference and displays a sample of randomly selected SDSS point sources with the same flux limits as used for selecting variable sources. The middle and bottom rows compare the distributions of this reference sample, shown as contours, to the distributions of candidate variable sources, shown as dots.

The distributions of candidate variable sources and those of the reference sample are different, demonstrating that the candidate variables are *not* randomly selected from the whole sample. The most obvious difference between the distributions is a much higher fraction of quasars (recognized by their UV excess, $u - g < 0.6$) in the variable sample (quasars are known to be variable on long time scales discussed here, see §5). Another notable difference is a presence of RR Lyrae stars ($u - g \sim 1.2$, $g - r \sim 0$) among the candidate variables. Thus, known variable sources indeed dominate the selected candidates.

In order to quantify these differences, as well as those in other parts of the color-color diagram, we divide color-color diagrams into seven characteristic regions, each dominated by a particular type of source (for more details about the distribution of point sources in SDSS color-color diagrams see Lenz et al. 1998, Fan 1999, Finlator et al. 2001, and Richards et al. 2002). The fractions of variable and all sources in each region are listed in Table 4. Notably, the fraction of variable sources which are found in region II, representative of numerous low-redshift quasars, is ~ 35 times higher than for the reference sample¹⁷. The corresponding fraction for region VII (which includes high-redshift quasars and, possibly, variable stars) is even higher (~ 150), but the statistics are less robust due to a smaller number of sources. Another quantitative representation of the color differences introduced by the variability requirement is shown for $u - g$ color in Fig. 15. These, and other differences listed in Table 4, demonstrate that the sample of selected candidate variables is **not** dominated by spurious objects.

The fraction of selected candidate variables across the sky is stable, and, in particular, does not depend on the stellar number density, nor shows jumps at the boundaries of

¹⁷The fraction of low-redshift quasars is higher for blue selection because the DPOSS faint cutoff is brighter in the red band (see Table 3).

Schmidt plates. Figure 16 illustrates this stability for a 2.5 deg. wide strip centered on the Celestial Equator, where the fraction of candidate variables remains $\sim 0.8\%$ (not corrected for unknown selection incompleteness), despite the stellar counts varying by a factor of ~ 3 (a slight increase at $RA \sim 230$ is caused by RR Lyrae in the Sgr dwarf tidal stream, see Section 4).

3.2.2. *The Comparison with Repeated SDSS Imaging Observations*

The analysis presented in the previous section shows that the selected candidate variables are not dominated by spurious sources. Here we obtain a quantitative estimate of the selection efficiency using repeated SDSS imaging data. For about 10% of the sky area analyzed here (the SDSS southern equatorial strip, see York et al. 2000), there exist between 6 and 9 epochs of SDSS imaging, obtained over a period of four years. Both due to a larger number of epochs and to more accurate photometry (~ 0.02 mag, for details see Ivezić et al. 2003b), these data have a much higher completeness and efficiency for discovering variable sources than the photographic/SDSS presented here. We select variable sources from repeated SDSS scans by requiring an rms variability larger than 0.03 mag in the g band. This selection results in a negligible fraction of spurious candidates ($< 1\%$), a high completeness (for example, more than 90% for RR Lyrae stars), and is also sensitive to long-period variables and quasar variability. About 7% of point sources brighter than $g = 19$ pass the adopted selection cut (for details see Ivezić et al. 2004, in prep).

Using the SDSS-DPOSS G-band candidates selected by relaxed criteria (see entry 5 in Table 3), we find that repeated SDSS scans (at least 6 epochs) exist for 955 sources. About half of these (49%) are confirmed as variable by SDSS data. The SDSS-POSS candidate variables not confirmed as variables by multi-epoch SDSS data tend to be at the faint end and have smaller SDSS-POSS magnitude differences than the confirmed variables. Thus, the sample efficiency can be further increased by a more restrictive selection requiring $g < 19$ and other cuts listed as entry 7 in Table 3. This selection results in 51 SDSS-DPOSS candidate variables with multi-epoch SDSS data; 73% are confirmed as variable. The distributions of confirmed and spurious SDSS-DPOSS variables in SDSS color-color diagrams are compared in Fig. 17. It is not surprising that most of the spurious SDSS-DPOSS variables are found in the stellar locus, because for a given contamination fraction (which is not expected to be a strong function of color) most of the contaminants come from the most populated part of the diagram. Repeating this analysis separately for sources from inside and outside the stellar locus, we find that the fraction of true variable sources among the selected candidates from the locus is 54%, while outside the locus it is as

high as 94%. Assuming that no more than 10% of sources from the locus are truly variable, the former fraction implies that the decision to tag a source as a candidate variable is correct in more than 95% of cases (for $g < 19$).

3.2.3. *The Large-amplitude Variables and Visual Comparison of Images*

The presumed large amplitude variables ($\gtrsim 1$ mag) may be more likely to be spurious (e.g. due to various defects on photographic plates). This possibility cannot be robustly tested using methods from the previous section due to insufficient number of sources. On the other hand, presumed variations with such a large amplitude can be tested by the visual comparison of SDSS and POSS images. The distribution of 70 SDSS-DPOSS candidates with $0.7 < \Delta G < 1$ and 24 candidates with $1 < \Delta G < 3$ in SDSS color-color diagrams is shown in Fig. 18. As evident, their distribution does not follow the distribution for the reference sample, indicating that they are not dominated by spurious candidates. We have visually inspected POSS and SDSS images for these 94 candidates and found that only ~ 30 may have been affected by nearby bright stars. Additional visual inspection of large amplitude variables selected using the USNO-A2.0 catalog recovered a spectacular case shown in the top panel in Fig. 19. After analyzing the plate print, as well as the brightness profiles, we concluded that the two bright POSS sources were an artefact¹⁸ (probably caused by splattered liquid on the POSS plate). While this is a disappointing outcome, it, nevertheless, vividly demonstrates the ability of the selection method to recognize differences between POSS and SDSS data. Another example of a spurious candidate is shown in the bottom panel in Fig. 19. Due to a nearby star, which happened to be a large proper motion object, the candidate’s POSS photometry was noticeably affected, while the more accurate SDSS photometry reported a single object with a correct magnitude.

Despite these pitfalls, the SDSS-POSS comparison does yield true large amplitude variables. For example, one of the sources with an SDSS-POSS magnitude difference of ~ 2 mag is in the region multiply observed by SDSS (12 epochs). The available SDSS data demonstrate that it is a long-period variable with a peak-to-peak amplitude exceeding 5 mag (Ivezić et al. 2004, in prep). This star, and another example of a large-amplitude variable, are shown in Fig. 20.

¹⁸This is a good example of benefits afforded by large collaborations: they provide an increased statistical chance of working with a sufficiently senior member familiar with old technologies and all their pitfalls.

4. The Milky Way Halo Structure Traced by Candidate RR Lyrae Stars

As recently shown (Ivezić et al. 2000, Vivas et al. 2001, Ivezić et al. 2003cd), faint RR Lyrae stars have a very clumpy distribution on the sky (most prominent features are associated with the Sgr dwarf tidal stream). This substructure offers a test of the spatial homogeneity of the selection algorithm: the known clumps ought to be recovered to some extent by the candidate RR Lyrae stars selected here, if the selection algorithm is robust. Furthermore, if such robustness can be demonstrated, the SDSS-POSS candidates can be utilized to quantify the halo substructure in the areas of sky for which multi-epoch SDSS data do not exist.

4.1. The $u - g$ Color Distribution of Candidate RR Lyrae Stars

Before proceeding with the analysis of spatial distributions of candidate RR Lyrae stars, we test their selection robustness using a method introduced¹⁹ by Ivezić et al. (2000). RR Lyrae stars have somewhat redder $u - g$ color (~ 0.2 mag) than stars with similar effective temperature (i.e. $g - r$ color) that are not on the horizontal giant branch. Since the u band flux is not used in the selection of variable objects (all POSS bands are redder than the SDSS u band), this offset is a robust indication that the candidate variables are dominated by true RR Lyrae stars. Fig. 21 compares the $u - g$ color distribution for candidate variable objects to the distribution for all sources in a narrow $g - r$ range (0 to 0.05, designed to exclude the main stellar locus). As evident, the selected candidates have redder $u - g$ color than the full sample, in agreement with the color distribution of RR Lyrae selected using light-curves obtained by the QUEST survey (Ivezić et al. 2003a). The difference is more pronounced for the selection in blue bands (because the variability amplitude decreases with wavelength), and somewhat more pronounced for the GSC catalog than for the DPOSS catalog. The counts of selected candidates are consistent with the conclusion from the previous section that the decision to tag a source as a candidate variable is correct in more than 95% of cases.

We determined the selection completeness for RR Lyrae stars using a complete sample of 162 RR Lyrae stars discovered by the QUEST survey and discussed by Ivezić et al. (2003a). We find that 32 (20%) of these stars are recovered by the relaxed DPOSS G-band selected sample.

¹⁹This method was suggested to Ivezić et al. by the referee Abi Saha.

4.2. The Spatial Distribution of Candidate RR Lyrae Stars

Using the relaxed DPOSS G-band selected sample (GSC-based selection performs better, but the public catalog is not deep enough to probe the outer halo), we isolate 628 RR Lyrae candidates by adopting color boundaries from Ivezić et al. (2003a). The magnitude-position distribution of 350 candidates within 5 deg. from the Celestial Equator is shown in Fig. 22. The sample completeness is fairly uniform for $r < 19$ and decreases with r towards the selection faint limit of $r = 19.5$ (corresponding to ~ 60 kpc). The clumps easily discernible at $(\alpha_{2000}, r) \sim (210, 19.2)$ and at $(30, 17)$ are associated with the Sgr dwarf tidal stream. The clumps at $(180, 17)$ and at $(330, 17)$ have also been previously reported (Vivas et al. 2001, Ivezić et al. 2003c). The recovery of these known structures suggests that the clump at $(\sim 235, \sim 15.5)$, which has not been previously reported, is a robust detection. Another previously unrecognized clump is detected around $\alpha_{2000} \sim 240^\circ$ and $\delta_{2000} \sim 50^\circ$ (see Fig. 23). The significance of these newly recognized structures will be placed in a broader context of other available data elsewhere (Ivezić et al., 2004, in prep.).

5. The Long-term Variability of Quasars

The optical continuum variability of quasars has been recognized since their first optical identification (Matthews & Sandage 1963), and it has been proposed and utilized as an efficient method for their discovery (van den Bergh, Herbst, Pritchett 1973; Hawkins 1983; Hawkins & Veron 1995; Ivezić et al. 2003e). The observed characteristics of the variability of quasars are frequently used to constrain the origin of their emission (e.g. Kawaguchi et al. 1998, and references therein; Martini & Schneider 2003).

Recently, significant progress in the description of quasar variability has been made by employing SDSS data (de Vries, Becker & White 2003, hereafter dVBW; Vanden Berk et al. 2004, hereafter VB). The size and quality of the sample analyzed by VB (two-epoch photometry for 25,000 spectroscopically confirmed quasars) allowed them to constrain how quasar variability in the rest frame optical/UV regime depends upon rest frame time lag, luminosity, rest wavelength, redshift, the presence of radio and X-ray emission, and the presence of broad absorption line outflows. However, the time lags probed by the available SDSS data (up to 3 years) are too short to detect deviations of the structure function (the root-mean-square scatter of measured magnitudes, see Eq. 1 in dVBW) from a simple power-law that are expected for long time lags (Cid Fernandes, Sodré, & Vieira da Silva 2000, and references therein).

The much longer time lags between POSS and SDSS (~ 50 years in the observer's

frame) offer the possibility of detecting such deviations, despite larger photometric errors for the POSS catalogs, and to study the long-term characteristics of quasar variability. Using a recalibration approach similar to the one described here (except that only fields around known quasars were recalibrated), dVBW studied long-term variability for 3,791 quasars from the SDSS Early Data Release (Stoughton et al. 2002). Here we have assembled a larger sample of SDSS quasars ($\sim 17,000$, Schneider et al. 2003), which allows us to constrain the overall shape of the $m_{SDSS} - m_{POSS}$ distribution and not only its root-mean-square scatter, as discussed in the next section. The dependence of the long-term quasar variability on luminosity, rest-frame wavelength, and time lag is analyzed in the subsequent section.

5.1. The Distribution of SDSS-POSS Magnitude Differences for Quasars

Analysis of the multi-epoch SDSS imaging data suggests that the distribution of Δm for quasars is better described by an exponential distribution than by a Gaussian distribution, for all bands (*ugriz*) and time scales probed (up to 4 years time lag in the observer’s frame). This result is independent of whether the data are binned by wavelength and time lag in the rest or observer’s frame (Ivezić et al. 2004, hereafter I04, in prep). Here we investigate whether this result can be reproduced for much longer time lags using SDSS-POSS measurements.

Fig. 24 shows the magnitude difference distributions for stars and spectroscopically confirmed quasars with redshifts in the range $0.3 < z < 2.4$, measured using GSC, DPOSS, and USNO-A2.0 catalogs. The distributions for quasars are marked by triangles, and those for a control sample of stars with the same magnitude distribution²⁰ are marked by solid circles.

The dashed lines in Fig. 24 show exponential distributions that have the same rms scatter as the data (the rms for each distribution are shown in the panels, and also listed in Table 5), and the dot-dashed lines show Gaussian distributions, both convolved with a Gaussian of the same width as the distribution of magnitude differences for stars. While the data presented here do not constrain the tails of the Δm distributions as well as multi-epoch SDSS data (due to larger photometric errors), the obtained magnitude distributions are

²⁰The slope of the differential magnitude distribution (“number counts”) for quasars is much steeper than that for stars. Since the photometric errors increase with magnitude, care must be taken to properly account for the error contribution to the measurement of the structure function. A simple comparison of two magnitude-limited samples of stars and quasars results in an underestimated photometric error contribution to the structure function.

consistent with the inferences made using multi-epoch SDSS data. Typically, $\sim 1\%$ of the sample is outside the $\pm 3\sigma$ boundaries, a fraction about a five times larger than expected for a Gaussian distribution. While formally significant, it is possible that the remaining calibration problems with POSS catalogs have contributed to this deviation from a perfect Gaussian distribution. In any case, the deviations are sufficiently small for the rms width to be an efficient statistic for describing the observed distributions.

These observed rms values, listed in Table 5, are $\sim 1\sigma$ (~ 0.05 - 0.10 mag) smaller than the values obtained by dVBW. The photometric errors (i.e. structure function for stars) displayed in Fig. 8 from dVBW correspond to the smaller of the two curves shown in their Fig. 4. Adopting the other curve decreases the estimate of the quasar variability as measured by dVBW, and thus decreases the discrepancy with our results to a $< 1\sigma$ level. It is noteworthy that the magnitude difference distributions for stars shown in Fig. 24 have smaller rms values than do the structure functions for stars shown in Fig. 4 from dVBW (our values correspond to $\log(\text{SF}) \sim -0.65$ or less). Thus, it is plausible that the remaining slight discrepancy is due to somewhat different procedures used to recalibrate POSS catalogs.

5.2. The Turn-over in the Structure Function

The extrapolation of the power-law dependence of the quasar rms variability on time measured at short time scales using repeated SDSS imaging (I04) predicts that the quasar rms variability measured using SDSS and POSS I should be of the order 0.60 mag, and 0.35 mag for SDSS-POSS II. Since the measured values (see Table 5) are smaller than these extrapolated values, they present strong evidence for a turn-over in the quasar structure function.

Fig. 25 shows the dependence of structure function on rest-frame time lag, in the range 2000–3000 Å, for two data sets: SDSS-SDSS for short time lags (small symbols, I04; note that the variability inferred from repeated imaging scans is fully consistent with the results presented by VB, that were based on a comparison of imaging and spectrophotometric magnitudes), and SDSS-POSS for long time lags (large symbols). The extrapolation of the power law measured for short time scales (dashed line) clearly overestimates the amplitude of the structure function reported here. We fit the observed dependence of structure function on rest-frame time lag using the following functional form

$$SF(\Delta t_{RF}) = D \left(1 - e^{-(\Delta t_{RF}/\tau)^\gamma} \right) \quad (4)$$

The best fit parameters are $D = 0.32 \pm 0.03$, $\tau = (390 \pm 80)$ days, and $\gamma = 0.55 \pm 0.05$.

This best-fit is shown in Fig. 25 by the dot-dashed line. We conclude that *the characteristic time scale for optical variability of quasars is of the order 1 year in the rest frame*. We postpone a more detailed analysis to a forthcoming paper.

5.3. The Dependence of Long-term Variability on Luminosity, Rest-frame Wavelength and Time Lag

The distribution of time differences in the observer’s frame for SDSS-POSS variability measurements is strongly bimodal (~ 10 years for SDSS-POSS II and ~ 50 years for SDSS-POSS I comparison). However, the distribution of time lags measured in the quasar rest-frame is more uniform due to a wide distribution of redshifts (the $1 + z$ effect; for a discussion, see dVBW). The same effect also widens and flattens the distribution of rest-frame wavelengths. For the data discussed here, the rest-frame time lags span the range 1,200-13,500 days, and the rest-frame wavelength is limited to the range 1,400-4,800 Å (using the bluest two bands in each survey).

In this section we investigate whether the correlations of variability with luminosity and rest-frame wavelength observed for short time lags (VB, I04) are valid for long time lags. In particular, we examine whether the decrease of variability with luminosity and wavelength, and increase with time, are observed for large time lags.

The dependence of variability on numerous relevant parameters complicates the analysis, and has resulted in many conflicting results in the literature (for a summary see Giveon et al. 1999). Furthermore, many of these parameters are highly correlated in flux-limited quasar samples due to steep quasar “counts” (the differential apparent magnitude distribution). Nevertheless, the sample considered here is sufficiently large that some of these degeneracies can be lifted by simple binning, similarly to the analysis described by VB.

The top left panel in Fig. 26 shows the distribution of 7,279 quasars with $i < 19$, $G_{SDSS} < 19$, and redshifts in the range $0.3 < z < 2.4$, in the redshift vs. i band absolute magnitude plane (M_i , computed using the WMAP cosmological parameters, $\Omega_m = 0.27$, $\Omega_\Lambda = 0.73$, $h = 0.71$, and K-corrected using $F_\nu \propto \nu^{-0.5}$). Their distribution in the M_i vs. rest-frame wavelength plane is shown in the top right panel (the two overlapping distributions arise from the two POSS bands used in this analysis, O and E for POSS I, and G and R for POSS II).

We decouple the variability dependence on absolute magnitude and rest-frame wavelength by computing the structure function for objects selected in narrow bins, shown

in the top right panel in Fig. 26 by short-dashed lines (two bins with nearly constant M_i) and long-dashed lines (three bins with nearly constant λ). The symbols in each strip are used to mark the corresponding histograms in the lower four panels. The dependence of the structure function on rest-frame time lag is essentially the same as its dependence on rest-frame wavelength because the ratio of these two quantities is nearly constant ($\Delta t_{RF} \sim C \lambda_{RF}$), with $C \sim 0.8$ days/Å for SDSS-POSS II data, and $C \sim 3.2$ days/Å for SDSS-POSS I data (that is, λ_{RF} in the two lower right panels in Fig. 26 is nearly equal to $\Delta t_{RF}/C$).

The middle left panel shows the dependence of the structure function (computed using the definition from dVBW, and corrected for measurement errors) on M_i for SDSS-POSS II magnitude differences. The DPOSS bands (we used G and R bands in this analysis) produce consistent results, which agree well with the correlation $SF \propto 1 + 0.024 M_i$ (shown by the line), inferred by I04 from repeated SDSS imaging scans.²¹ The middle right panel shows the dependence of the structure function on the rest-frame wavelength. The data are fully consistent with a constant value, shown by the dashed line (0.24 mag, median of all the points). This behavior is in contrast with the relationship $SF \propto \lambda^{-0.3}$, derived from repeated SDSS imaging data (I04). However, this result is affected by the correlation in the SDSS-POSS II sample between rest-frame wavelength and time lag — the increase of variability with time for the rest-frame time lags probed (~ 1300 - 3400 days) offsets its decrease with rest-frame wavelength.

This effect is expected to be much weaker in SDSS-POSS I data due to a turn-over in the quasar structure function discussed in the previous section. Indeed, as the bottom two panels demonstrate, while the dependence of variability on M_i is still reproduced (albeit with larger errors), the variation of structure function with wavelength is consistent with $SF \propto \lambda^{-0.3}$. Note that we did not correct the data points for the systematic residual dependence on rest-frame wavelength in the two bottom left panels (the correction is ± 0.03 mag for the two edge bins, relative to the middle one), and on absolute magnitude in the two bottom right panels (relative offset between the two bins is 0.02 mag). We conclude that there is no evidence that the dependence of the structure function on luminosity and rest-frame wavelength is different for long time lags discussed here (4-40 years in the rest frame) than for shorter time lags (VB, I04). A more detailed analysis of these data is postponed to a future publication.

²¹This expression agrees well with the result from VB who used a different functional form to describe this correlation.

6. Discussion

We present a direct comparison of photometric measurements available in public POSS catalogs. The most accurate photometry is provided by the GSC2.2 catalog. The results of photometric recalibration based on a dense grid of calibration stars measured by the SDSS demonstrate that errors in POSS photometry can be reduced by about a factor of two. POSS I magnitudes can be brought to ~ 0.15 mag accuracy, and POSS II magnitudes to ~ 0.10 mag accuracy. While these apparently irreducible errors are considerably larger than those delivered by modern CCD data (~ 0.02), the POSS catalogs are, nevertheless, invaluable for studying sources variable on long time scales. A particular success of the recalibration method is that the resulting error distribution for POSS photometry is nearly Gaussian, which greatly helps in the design of robust algorithms for selecting candidate variable sources.

We designed and tested algorithms for selecting candidate variable sources using POSS and SDSS photometric measurements. The algorithm’s decision to tag a source as a candidate variable is correct in more than 95% of cases. The selection criteria can be tuned up to result in samples that contain no more than 30% of spurious candidates.

This is the first study that examined the distribution of sources variable on long time scales in SDSS color-color diagrams. Even with the fairly large cutoffs for selecting candidate variables (0.20-0.35 mag), we find that at least 1% of faint optical sources appear variable. About 10% of the variable population are quasars, although they represent only 0.25% of all point sources (for $g < 19$).

Using a sample of $\sim 17,000$ spectroscopically confirmed quasars, we demonstrate that the power-law increase of the quasar variability (structure function, rms) with time lag observed for short time lags cannot be extrapolated beyond a few years in the rest frame – such extrapolation predicts a variability level significantly larger than measured (0.35 vs. 0.60 mag for SDSS-POSS I, and 0.24 vs. 0.35 mag for SDSS-POSS II). The implied turn-over in structure function indicates that the characteristic time scale for optical variability of quasars is of the order 1 year in the rest frame. The long-term ($\gtrsim 1$ year) quasar variability decreases with luminosity and rest-frame wavelength similarly to the short-term ($\lesssim 1$ year) behavior.

A particularly valuable result of comparing POSS and SDSS catalogs is the selection of candidate RR Lyrae stars, which are excellent probes of the Milky Way’s halo structure. We demonstrated that the known halo substructures are recovered by the selected candidates, and discovered several new features. This method will eventually yield several thousand RR Lyrae candidates.

Our study also revealed some limitations of the POSS catalogs. In particular, we had to limit our search for variable sources to only isolated point sources detected by both POSS and SDSS. Attempts to find sources detected by only one survey, or variable sources that are blended with another nearby source, were unsuccessful due to overwhelmingly large numbers of false positives.

Despite these shortcomings, the assembled catalogs of candidate variable sources offer a good starting point for further analysis and follow-up observations. For example, light curves and spectra for selected candidates could be obtained even with telescopes of modest size. Such additional data would help improve candidates' classification beyond information provided by SDSS colors. Another potentially interesting research direction is positional cross-correlation with catalogs obtained at other wavelengths (e.g. ROSAT, 2MASS, IRAS). For example, long-period variables such as Mira and other AGB stars are typically strong infrared emitters, and thus could be efficiently separated from the rest of candidate variables.

This study once again demonstrates the importance of maintaining a careful archive of astronomical observations; the data may be valuable long after the acquisition technology becomes obsolete.

Acknowledgments

We thank Princeton University for generous financial support of this research.

Funding for the creation and distribution of the SDSS Archive has been provided by the Alfred P. Sloan Foundation, the Participating Institutions, the National Aeronautics and Space Administration, the National Science Foundation, the U.S. Department of Energy, the Japanese Monbukagakusho, and the Max Planck Society. The SDSS Web site is <http://www.sdss.org/>.

The SDSS is managed by the Astrophysical Research Consortium (ARC) for the Participating Institutions. The Participating Institutions are The University of Chicago, Fermilab, the Institute for Advanced Study, the Japan Participation Group, The Johns Hopkins University, Los Alamos National Laboratory, the Max-Planck-Institute for Astronomy (MPIA), the Max-Planck-Institute for Astrophysics (MPA), New Mexico State University, University of Pittsburgh, Princeton University, the United States Naval Observatory, and the University of Washington.

REFERENCES

- Abazajian, K., Adelman, J.K., Agueros, M., et al. 2003, *AJ*, 126, 2081
- Akerlof, C.W., Kehoe, R.L., McKay, T.A., et al. 2003, *PASP*, 115, 132
- Cid Fernandes, R., Sodré, L.Jr., & Vieira da Silva, L.Jr. 2000, *ApJ*, 544, 123
- de Vries, W.H., Becker, R.H., & White, R.L. 2003, *AJ*, 126, 1217
- Djorgovski, S.G., Gal, R.R., Odenwahn, S.C., de Carvalho, R.R., Brunner, R., Longo, G. & Scaramella, R. 1998, in *Wide Field Surveys in Cosmology*, Editions Frontiers, p. 89 (also astro-ph/9809187)
- Eyer, L. 1999, *Baltic Astronomy*, 8, 321
- Fan, X. 1999, *AJ*, 117, 2528
- Finlator, K., Ivezić, Ž., Fan, X., et al. 2000, *AJ*, 120, 2615 (F00)
- Fukugita, M., Ichikawa, T., Gunn, J.E., Doi, M., Shimasaku, K., & Schneider, D.P. 1996, *AJ*, 111, 1748
- Giveon, U., Maoz, D., Kaspi, S., Netzer, H., & Smith, P.S. 1999, *MNRAS*, 306, 637
- Gunn, J.E., Carr, M., Rockosi, C., et al. 1998, *AJ*, 116, 3040
- Hawkins, M.R.S., & Veron, P. 1995, *MNRAS*, 275, 1102
- Hawkins, M.R.S. 1983, *MNRAS*, 202, 571
- Hawley, S.L., Covey, K.R., Knapp, G.R., et al. 2002, *AJ*, 123, 3409
- Helmi, A., Ivezić, Ž., Prada, F., et al. 2003, *ApJ*, 586, 195
- Hogg, D.W., Finkbeiner, D.P., Schlegel, D.J. & Gunn, J.E. 2002, *AJ*, 122, 2129
- Huber, M.E., Howell, S.B., Everett, M.E. & Groot, P.J. 2002, *BAAS*, 200, 5801
- Ivezić, Ž., Goldston, J., Finlator, K., et al. 2000, *AJ*, 120, 963
- Ivezić, Ž., Tabachnik, S., Rafikov, R., et al. 2001, *AJ*, 122, 2749
- Ivezić, Ž., Vivas, A.K., Lupton, R.H. & Zinn, R. 2003a, submitted to *AJ*, (also astro-ph/0310565)

- Ivezić, Ž., Lupton, R.H., Anderson, S., et al. 2003b, Proceedings of the Workshop *Variability with Wide Field Imagers*, Mem. Soc. Ast. It., 74, 978 (also astro-ph/0301400)
- Ivezić, Ž., Lupton, R.H., Schlegel, D., et al. 2003c, Proceedings of “Satellites and Tidal Streams”, May 26-30, 2003, La Palma, Spain (also astro-ph/0309075)
- Ivezić, Ž., Lupton, R.H., Schlegel, D., et al. 2003d, Proceedings of “Milky Way Surveys: The Structure and Evolution of Our Galaxy”, June 15-17, 2003, Boston (also astro-ph/0309074)
- Ivezić, Ž., Lupton, R.H., Johnston, D.E., et al. 2003e, Proceedings of “AGN Physics with the SDSS”, Richards, G.T. & Hall, P.B., eds., in press (also astro-ph/0310566)
- Kaiser, N., Aussel, It., Burke, B.E., et al. 2002, in “Survey and Other Telescope Technologies and Discoveries”, Tyson, J.A. & Wolff, S., eds. Proceedings of the SPIE, 4836, 154
- Kawaguchi, T., Mineshige, S., Umemura, M., & Turner, E.L. 1998, ApJ, 504, 671
- Lattanzi, M. G., & Bucciarelli, B. 1991, A&A, 250, 565
- Lenz, D.D., Newberg, J., Rosner, R., Richards, G.T., Stoughton, C. 1998, ApJS, 119, 121
- Lupton, R.H., Ivezić, Ž., Gunn, J.E., Knapp, G.R., Strauss, M.A. & Yasuda, N. 2003, in “Survey and Other Telescope Technologies and Discoveries”, Tyson, J.A. & Wolff, S., eds. Proceedings of the SPIE, 4836, 350
- Martini, P., & Schneider, D.P. 2003, ApJ, 597, L109
- Matthews, T.A., & Sandage, A.R. 1963, ApJ, 138, 30
- Minkowski, A., & Abel, G. O. 1963, in Stars and Stellar Systems, Vol. 3
- McLean, B.J., Greene, G.R., Lattanzi, M.G., & Pirenne, B. 2000, Astronomical Data Analysis Software and Systems IX, ASP Conference Series, Vol. 216, p. 145, N. Manset, C. Veillet and D. Crabtree, eds.
- Monet, D.G., Levine, S.E., Canzian, B., et al. 2003, AJ, 125, 984
- Munn, J.A., Monet, D.G., Levine, S.E., et al. 2004, AJ, in press
- Oke, J.B., & Gunn, J.E. 1983, ApJ, 266, 713
- Paczyński, B. 1996, astro-ph/9609073
- Paczyński, B. 2000, PASP, 112, 1281

- Paczynski, B. 2001, astro-ph/0110388
- Pier, J.R., Munn, J.A., Hindsley, R.B., Hennesy, G.S., Kent, S.M., Lupton, R.H. & Ivezić, Ž. 2003, AJ, 125, 1559
- Reid, I.N., Brewer, C., Brucato, R.J., et al. 1991, PASP, 103, 661
- Richards, G.T., Fan, X., Newberg, H.J., et al. 2002, AJ, 123, 2945
- Schlegel, D., Finkbeiner, D.P. & Davis, M. 1998, ApJ500, 525
- Schneider, D.P., Fan, X., Hall, P.B., et al. 2003, AJ, 126, 2579
- Smith, J.A., Tucker, D.L., Kent, S.M., et al. 2002, AJ, 123, 2121
- Stoughton, C., Lupton, R.H., Bernardi, M., et al. 2002, AJ, 123, 485
- Trevese, D., Kron, R.G., & Bunone, A. 2001, ApJ, 551, 103
- Tyson, J.A. 2002, in “Survey and Other Telescope Technologies and Discoveries”, Tyson, J.A. & Wolff, S., eds. Proceedings of the SPIE, 4836, 10
- Udalski, A., Zebrun, K., Szymanski, M., et al. 2002, Acta Astronomica, 52, 115 VizieR
On-line Data Catalog: I/246. Originally published in: U.S. Naval Observatory, Washington D.C. (1997)
- Urban, S.E., Corbin, T.E., & Wycoff, G.L. 1997, The ACT Reference Catalog, VizieR
Online Data Catalog, Originally published in: U.S. Naval Observatory, Washington D.C. (1997)
- van den Bergh, S., Herbst, E. & Pritchett, C. 1973, AJ, 78, 375
- Vanden Berk, D.E., Wilhite, B.C., Kron, R.G., et al. 2004, ApJ, in press, (also astro-ph/0310336)
- Vestrand, W.T., Borozdin, K., Brumby, S., et al. 2002, in “Advanced Global Communications Technologies for Astronomy II”, Kibrick, R.I., ed. Proceedings of the SPIE, 4845, 126 (also astro-ph/0209300)
- Vivas, A.K., Zinn, R., Andrewi, P., et al. 2001, ApJ, 554, L33
- Yanny, B., Newberg, H.J., Kent, S., et al. 2000, ApJ, 540, 825
- Woźniak, P.R., Udalski, A., Szymanski, M., Kubiak, M., Pietrzynski, G., Soszynski, I. & Zebrun, K. et al. 2002, Acta Astronomica, 52, 129

York, D.G., Adelman, J., Anderson, S., et al. 2000, AJ, 120, 1579

Appendix A: An Overview of POSS Catalogs Used in This Work

USNO catalogs

USNO-A2.0 is a catalog of 526,280,881 stars, based on a re-reduction of the Precision Measuring Machine (PMM) scans of Palomar Observatory Sky Survey I (POSS-I; Minkowski & Abel 1963) O and E plates, the UK Science Research Council SRC-J survey plates, and the European Southern Observatory ESO-R survey plates. For field centers with $\delta > -30^\circ$, data come from POSS-I plates, while data for field centers with $\delta < -35^\circ$ come from SRC-J and ESO-R plates. USNO-A2.0 catalog uses the ICRF as realized by the USNO ACT catalog (Urban et al. 1997), and in addition to source coordinates, it lists the blue (O) and red (E) magnitudes for each object. The USNO-B catalog (Monet et al. 2003), currently released in version 1.0, is the next in a sequence of catalogs produced²² by the USNO team. It is an all-sky catalog with positions, proper motions, magnitudes in different optical bands (O , E , J , F , N), and star/non-star estimator for approx. 1 billion objects. Beside the first epoch surveys (POSS-I, ESO-R, SRC-J), it also utilizes the second epoch surveys: POSS-II for field centers with $\delta > -30^\circ$, and SES (South Equatorial Survey) for $\delta < -35^\circ$ (Reid et al. 1991). It is fairly complete to $V = 21$, with the claimed astrometric accuracy of $0.2''$ (J2000), photometric accuracy of 0.3 mag, and 85% accuracy for distinguishing stars from non-stellar objects.

The Guide Star Catalog

The GSC II (McLean et al. 2000) is an all-sky catalog based on scans of the photographic plates obtained by the Palomar and UK Schmidt telescopes. Schmidt plates for both the Northern (POSS-II) and Southern (SES) hemisphere surveys were digitized on the GAMMA scanning machines. Positions, magnitudes, and classifications are produced for all objects on each plate and the data is stored in the COMPASS database. The GSC2.2 catalog is an all-sky, magnitude-selected export of calibrated source parameters from the COMPASS database, complete to $F = 18.5$ mag and $J = 19.5$ mag. It uses ~ 1000 objects per plate for astrometric calibration, resulting in astrometric errors of $0.3''$, and ~ 100 objects per plate for photometric calibration, resulting in errors in the range 0.2–0.25 mag. The number of unique objects exported is approximately 456 million²³.

²²Available from <http://www.nofs.navy.mil>

²³For more details and access to catalogs see <http://www-gsss.stsci.edu/gsc/GSHome.htm>

Digital Palomar Observatory Sky Survey (DPOSS)

The Digital Palomar Observatory Sky Survey (DPOSS; Djorgovski et al. 1998) is a digital version of the Second Palomar Observatory Sky Survey (POSS-II), based on the plate scans done at STScI, CCD calibrations done at Palomar, and processing done at Caltech. DPOSS consists of the original image database (~ 3 TB of pixel data) and the derived catalogs and metadata, primarily the Palomar-Norris Sky Catalog (PNSC). DPOSS is a survey of the northern sky ($\delta > -3^\circ$), in 3 bands (photographic J, F, N , calibrated to g, r, i ; note that we use upper case letters for DPOSS magnitudes to distinguish them from SDSS magnitudes), with typical limiting magnitudes $G \sim 21 - 21.5$, $R \sim 21$, and $I \sim 19.5$ mag. Accurate star-galaxy classification is available for all objects to $\sim 1 - 1.5$ mag above the detection limit²⁴. The initial data release covers the high Galactic latitudes. The final catalog is expected to contain about 50 million galaxies and a billion stars.

²⁴The survey and selected data products are publicly available from <http://dposs.caltech.edu>

Table 1. Best-fit Coefficients for
POSS-SDSS Photometric
Transformations

Band	b	c	σ
O_a	0.354	-0.32	0.26
E_a	-0.101	-0.30	0.25
O	0.444	0.05	0.31
E	-0.162	-0.29	0.27
J	0.075	0.10	0.32
F	-0.133	-0.14	0.20
N	-0.530	-0.37	0.25
J_g	0.105	0.20	0.14
F_g	-0.101	-0.18	0.10
G	-0.392	-0.28	0.20
R	-0.127	0.10	0.17

^aFor the definitions of b and c see eq. (1). The fourth column (σ) lists the residual rms scatter.

Table 2. Summary of Improvements in POSS Photometry

Catalog	σ_O^{old}	σ_O^{new}	σ_E^{old}	σ_E^{new}	σ_J^{old}	σ_J^{new}	σ_F^{old}	σ_F^{new}	σ_N^{old}	σ_N^{new}
USNO-A2.0	0.260	0.154	0.248	0.171	—	—	—	—	—	—
USNO-B1.0	0.294	0.137	0.294	0.149	0.311	0.112	0.201	0.116	0.261	0.175
GSC2.2	—	—	—	—	0.138	0.076	0.101	0.091	—	—
DPOSS ^b	—	—	—	—	0.189	0.086	0.162	0.112	—	—

^a“Old” refers to rms scatter before recalibration, and “new” to rms scatter after recalibration.

^b J and F bands listed for DPOSS correspond to G and R bands

Table 3. The Number of Selected Candidate Variables

band	$ \Delta m _{min}^a$	$ \Delta m/\sigma _{min}^b$	m_{faint}^c	N_{sel}^d
O	0.35	2.5	19.0	25,112
E	0.35	2.5	18.0	16,080
J	0.20	2.5	18.0	6,026
F	0.20	2.5	17.5	14,755
G	0.20	2.5	19.5	10,824
R	0.20	2.5	18.5	7,889
G ^e	0.30	3.5	19.0	1,112
R ^e	0.30	3.5	18.5	1,066

^aThe minimum value of magnitude change

^bThe minimum value of magnitude change normalized by the estimated photometric error

^cThe adopted faint limit (using synthesized SDSS magnitudes)

^dThe number of selected candidate variables in SDSS DR1 area (2099 deg²)

^eRestricted SDSS-DPOSS selection (see Section 3.2.2), magnitude limit corresponds to SDSS *g* band. There are $\sim 1.4 \times 10^6$ isolated point sources brighter than the same magnitude limit in the analyzed area.

Table 4. The distribution of variable sources in the $g - r$ vs $u - g$ diagram

Region ^a	Name ^b	% all ^c	% var _G ^d	% var _R ^e	all/var _G
I	white dwarfs	0.13	0.45	0.09	3.34
II	low- z QSOs	0.43	18.6	3.38	42.8
III	binary stars	0.10	6.21	1.13	61.6
IV	RR Lyrae	0.76	11.3	9.66	14.9
V	blue stars	75.7	47.8	53.4	0.63
VI	red stars	22.9	16.0	25.6	0.70
VII	high- z QSOs	0.02	2.43	7.32	132.7

^aThe regions boundaries are shown in Fig. 14

^bAn approximate description of the dominant source type

^cFraction of all SDSS sources in the region (based on run 752)

^dFraction of G-selected candidate SDSS-DPOSS variable sources in the region, restricted selection from Table 3

^eFraction of R-selected candidate SDSS-DPOSS variable sources in the region, restricted selection from Table 3

Table 5. The Long-Term Quasar Variability

band	rms ^a	error ^b	σ^c
J	0.24	0.08	0.23
F	0.23	0.11	0.20
G	0.25	0.10	0.23
R	0.28	0.14	0.24
O	0.47	0.20	0.42
E	0.37	0.18	0.32

^aThe rms scatter for quasars

^bThe rms scatter for stars with similar magnitude distribution as the selected quasars

^cAn estimate for the intrinsic rms variability of quasars,
 $\sigma = \sqrt{rms^2 - error^2}$

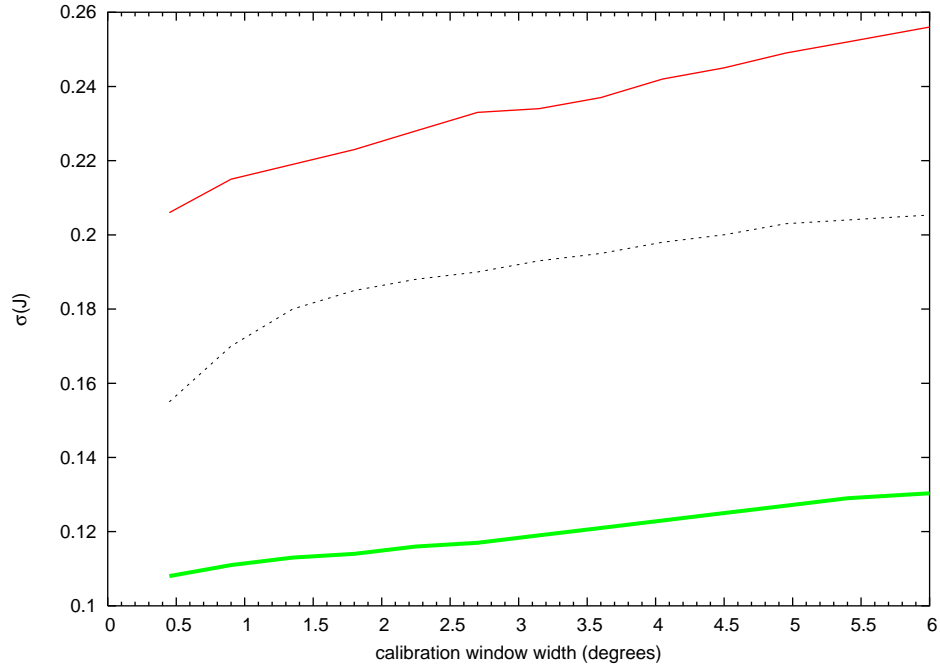


Fig. 1.— Photometric accuracy as a function of the recalibration window width for three POSS-II J plates. The decrease of the window width decreases photometric errors as expected. Note that when extrapolating curves to zero window width, plates show varying photometric accuracy, reflecting different intrinsic properties. The estimated improvement in accuracy by decreasing the window width from $\sim 0.5^\circ$ to 0 is only ~ 0.01 - 0.02 mag.

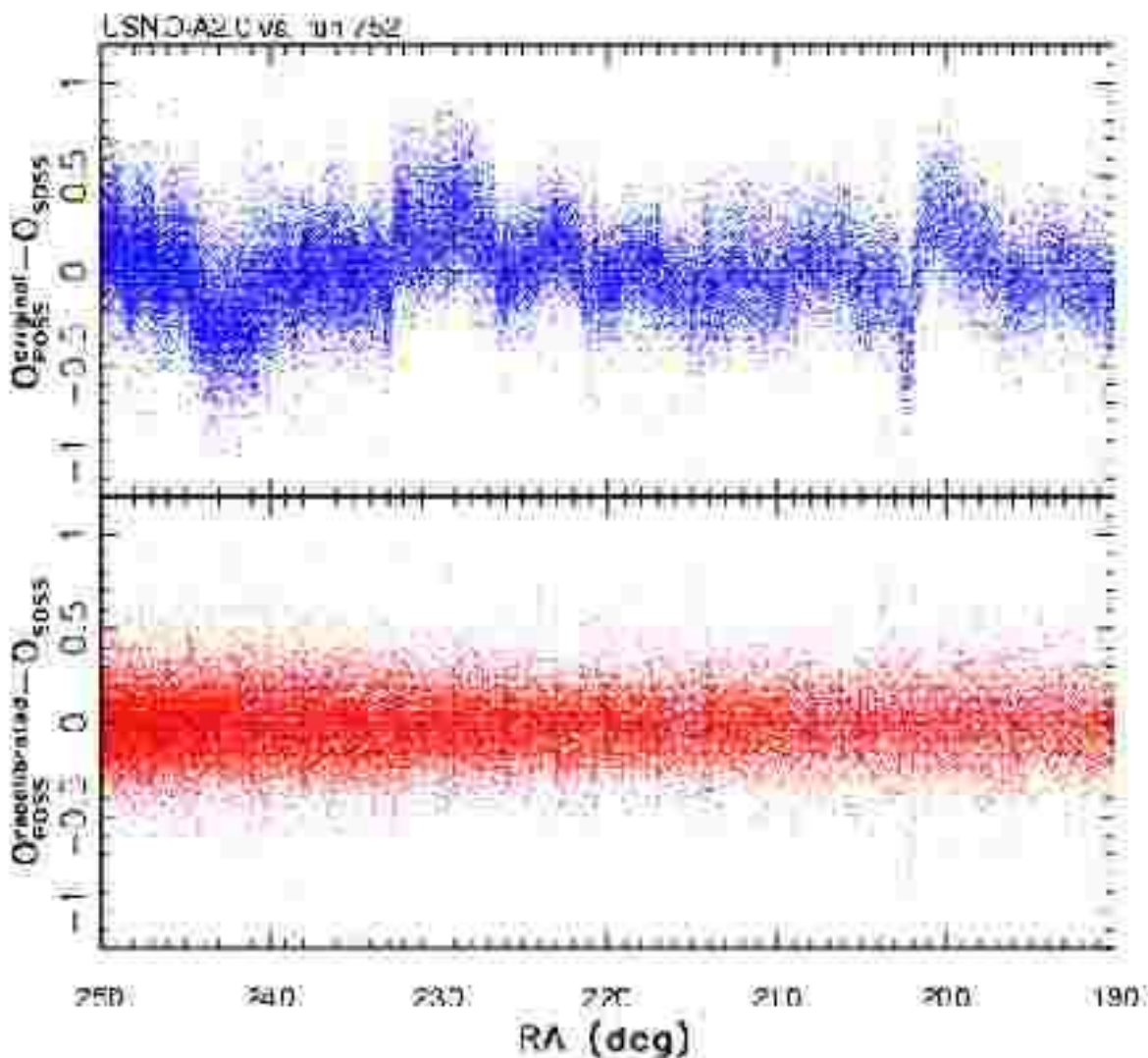


Fig. 2.— An illustration of the systematic photometric errors in POSS I catalogs, and of improvements made possible thanks to a dense grid of calibration stars provided by SDSS. The top panel shows the differences between the original USNO-A2.0 O magnitudes and synthetic SDSS-based O magnitudes for isolated stars with $O_{SDSS} < 18.5$, from a narrow equatorial strip (SDSS run 752, $|Dec| < 1.25$). Note the large jumps at the boundaries of 6 degree wide Schmidt plates. The bottom panel shows the differences between the recalibrated USNO-A2.0 O magnitudes and synthetic SDSS-based O magnitudes for the same stars.

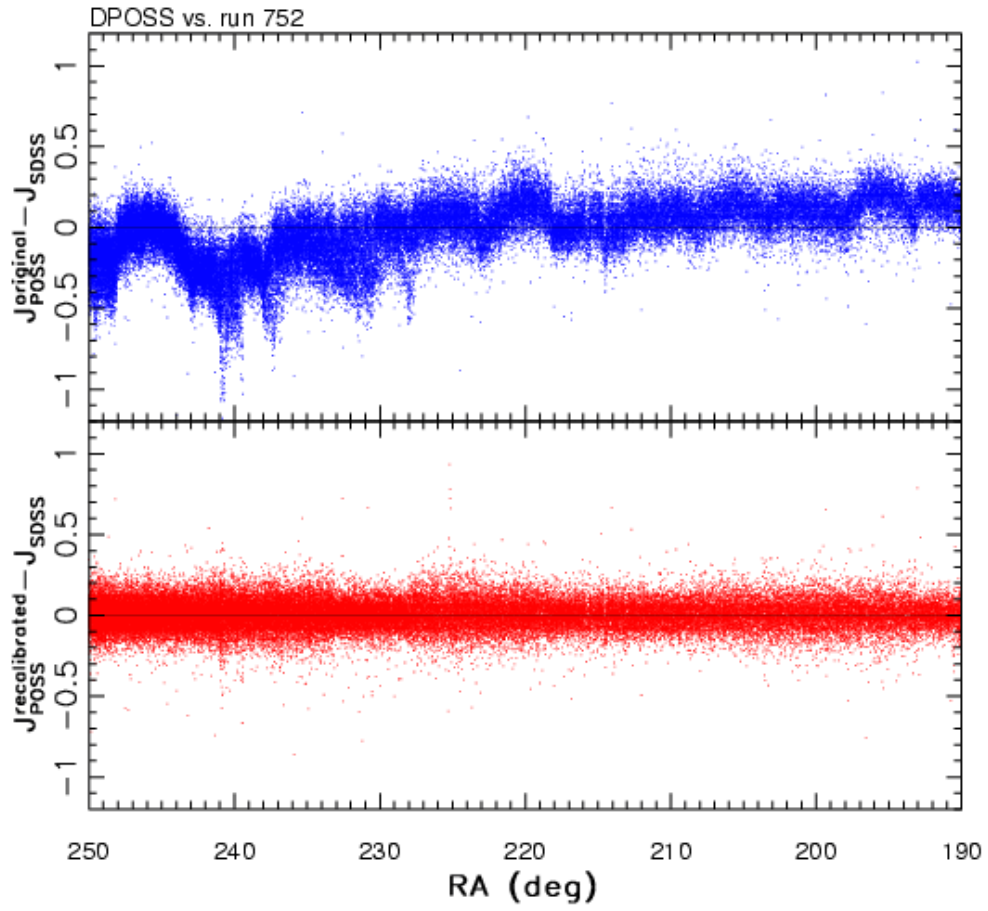


Fig. 3.— Same as Fig. 2, except that the G magnitudes taken from a POSS II-based DPOSS catalog are shown.

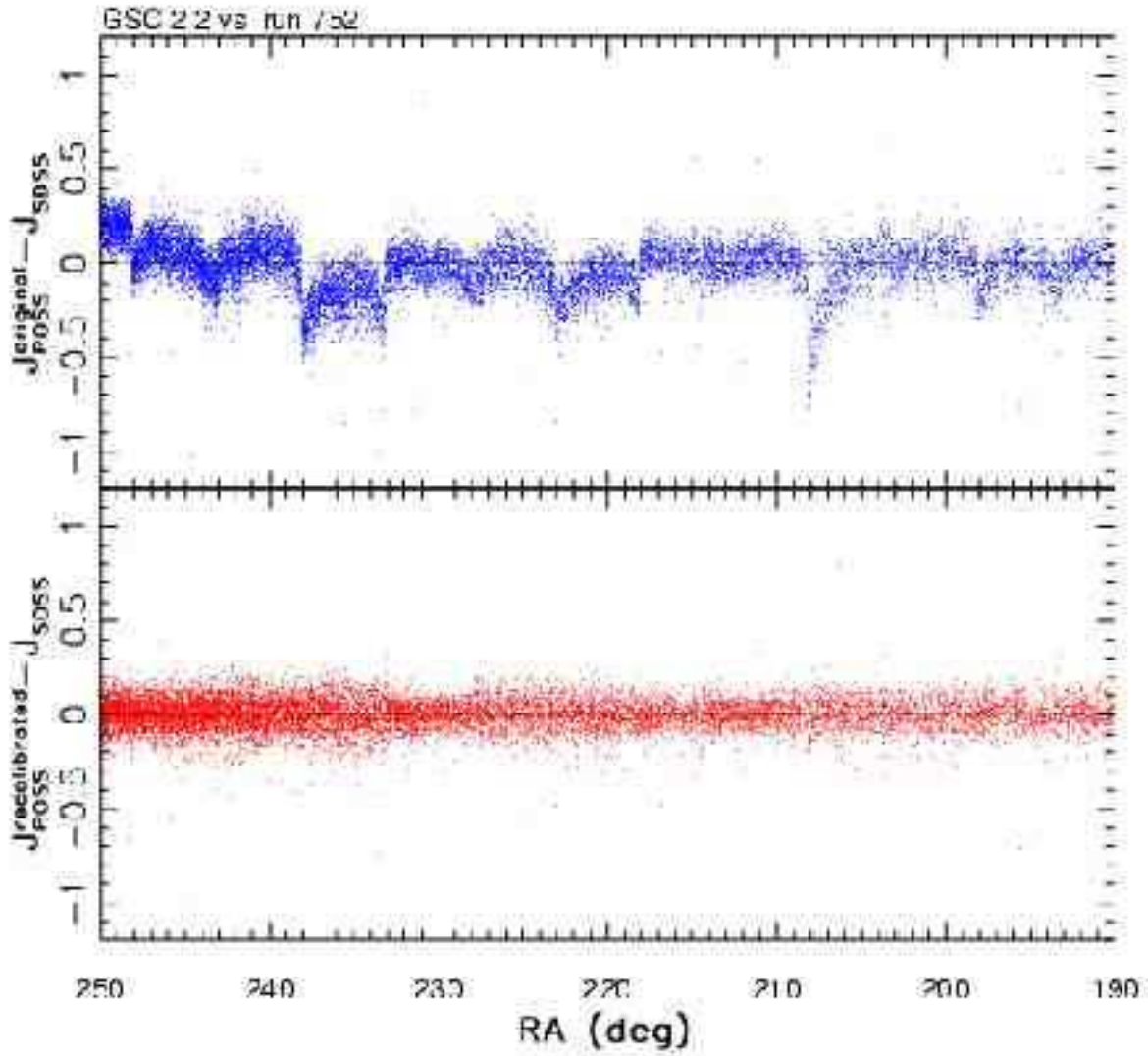


Fig. 4.— Same as Fig. 2, except that the J magnitudes taken from a POSS II-based GSC2.2 catalog are shown.

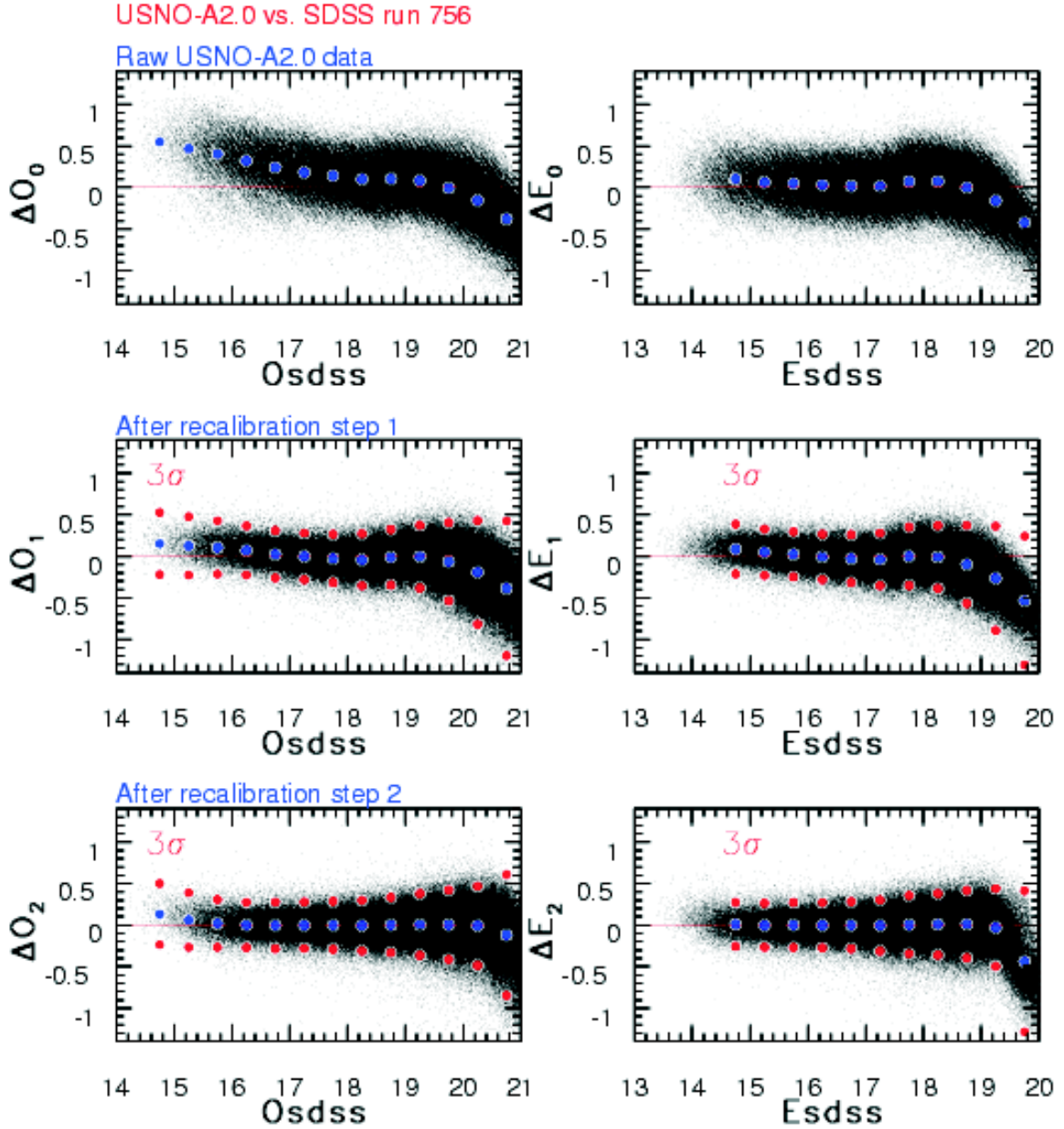


Fig. 5.— The illustration of the recalibration method for the USNO-A2.0 catalog. The dots in the top panels represent magnitude differences between the original POSS O (left column) and E (right column) magnitudes and the synthetic SDSS-based O and E magnitudes, as a function of the latter, for about 300,000 stars observed in ~ 100 deg² of sky in SDSS run 752. The middle panel shows the magnitude differences after the first recalibration step, where color-term and zero-point systematic errors are removed. The results of the second recalibration step, which removes the dependence of magnitude differences on magnitude, are shown in the bottom panels. The middle set of large symbols in each panel shows the median differences in magnitude bins, and the two outer sets of large symbols show equivalent Gaussian widths (determined from the interquartile range), multiplied by 3.

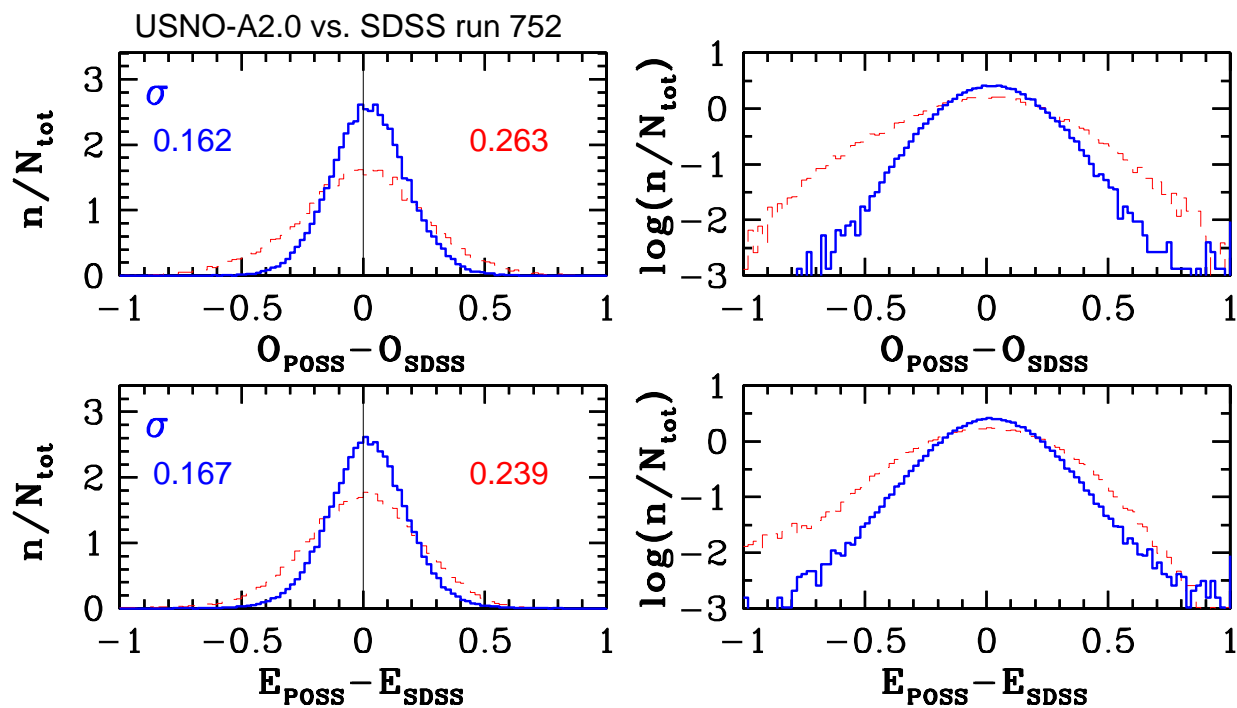


Fig. 6.— The improvements in photometric errors after recalibration for the USNO-A2.0 catalog. The POSS-SDSS magnitude differences before recalibration are shown by thin lines, and those after recalibration by thick lines. The left column shows error distribution on a linear scale, and the right column on a logarithmic scale. The equivalent Gaussian widths, determined from the interquartile range, are also shown in each panel (right: before, left: after).

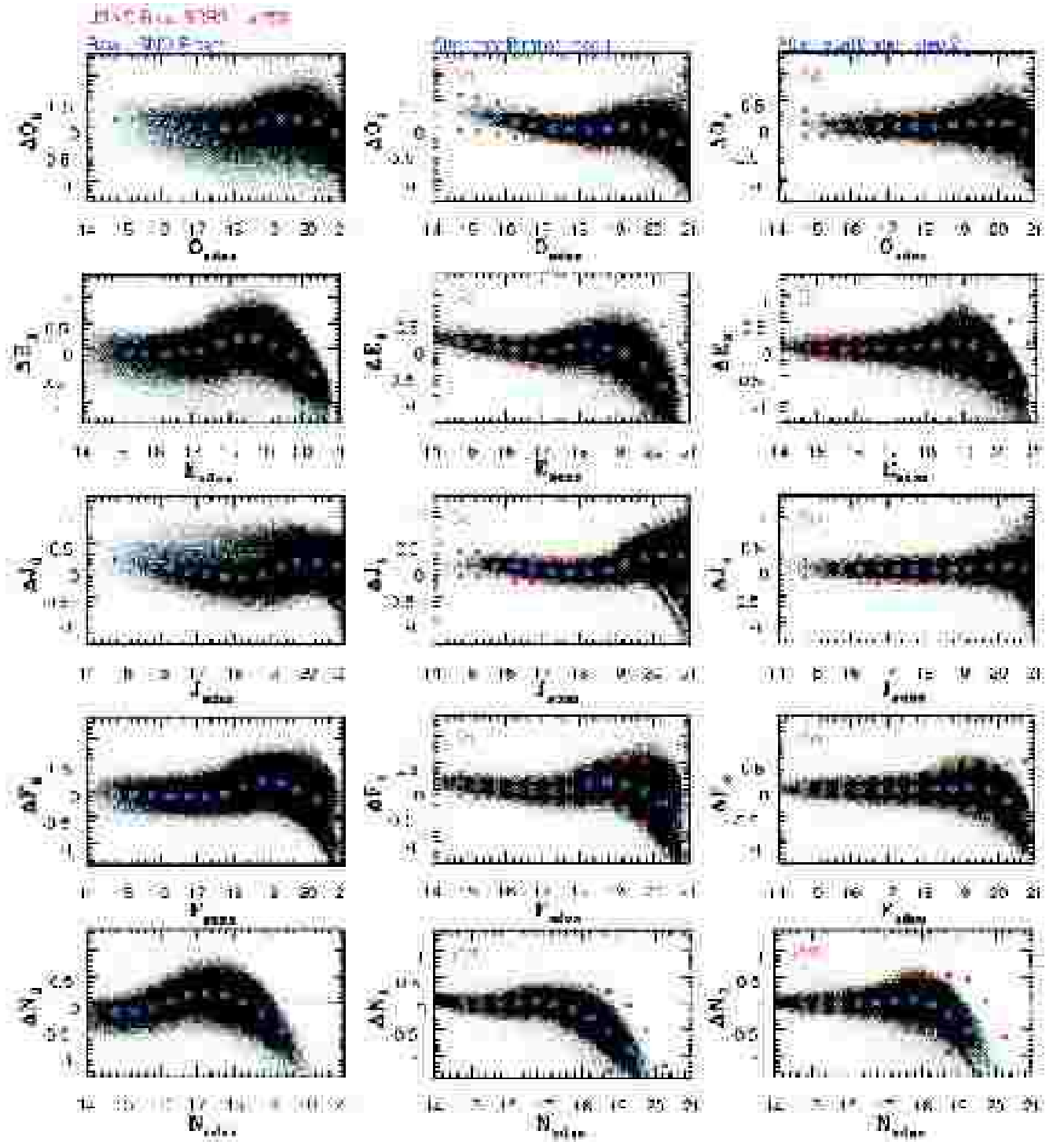


Fig. 7.— Same as Fig. 5, except for the USNO-B1.0 catalog.

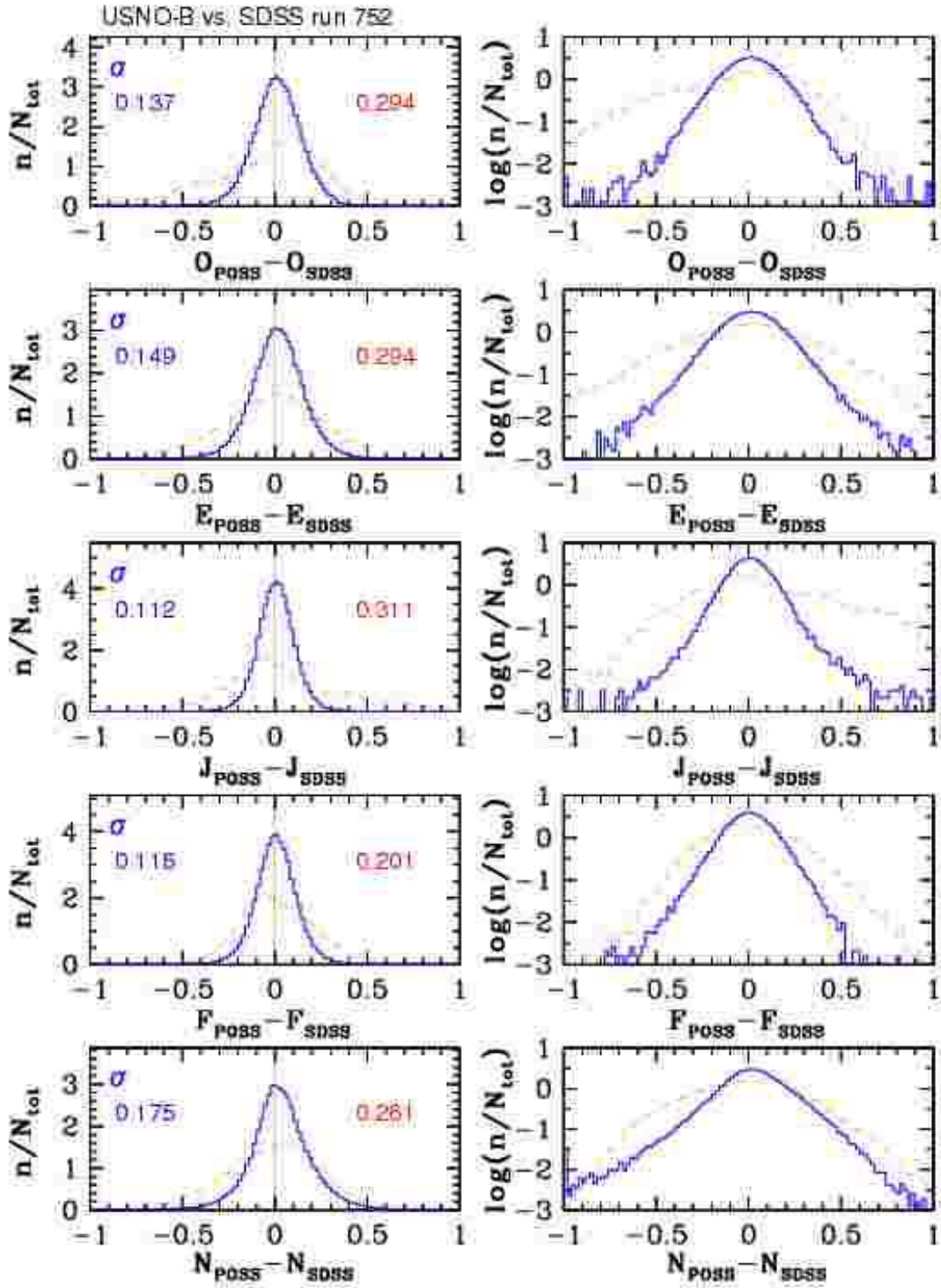


Fig. 8.— Same as Fig. 6, except for the USNO-B1.0 catalog.

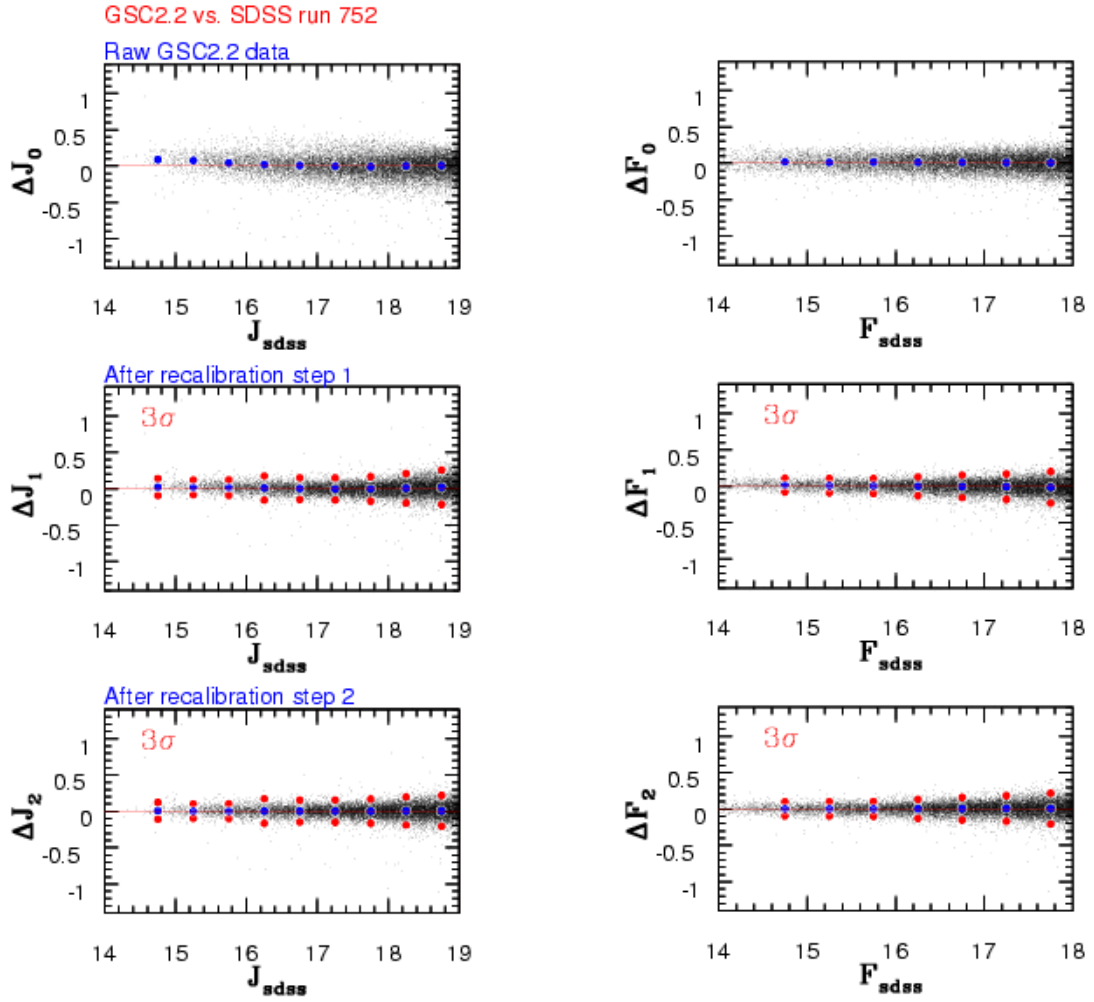


Fig. 9.— Same as Fig. 5, except that only the first recalibration step is shown, for the GSC2.2 catalog.

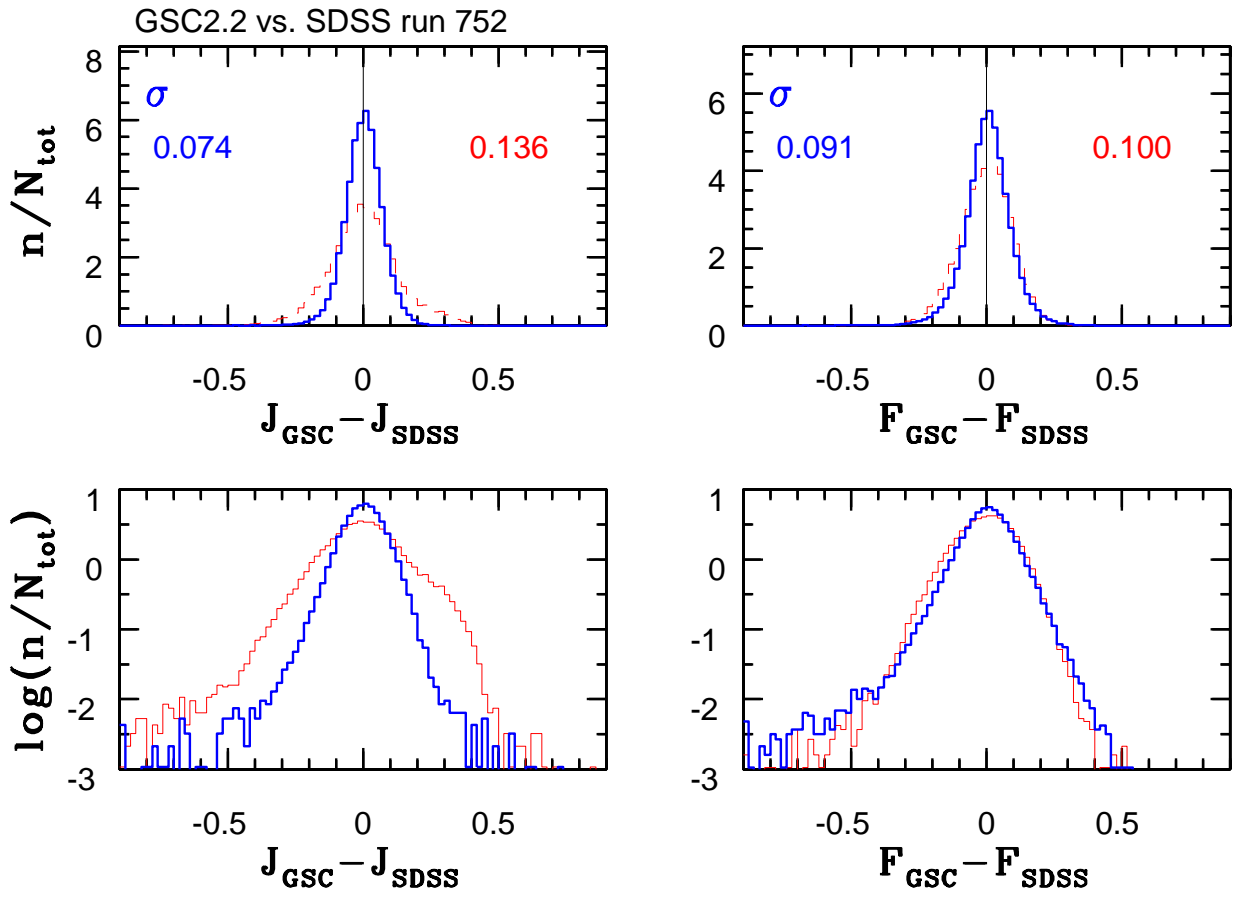


Fig. 10.— Same as Fig. 6, except for the GSC2.2 catalog.

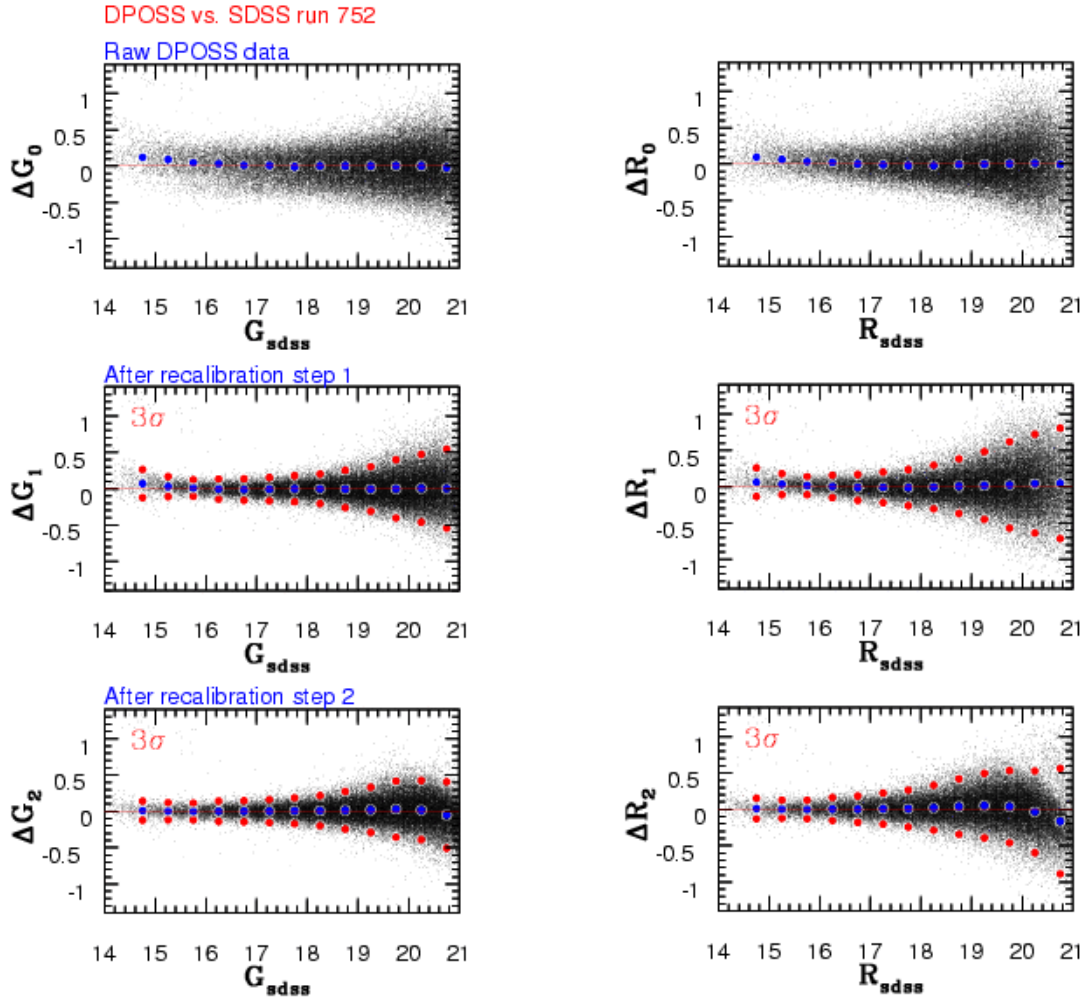


Fig. 11.— Same as Fig. 5, except for the DPOSS catalog.

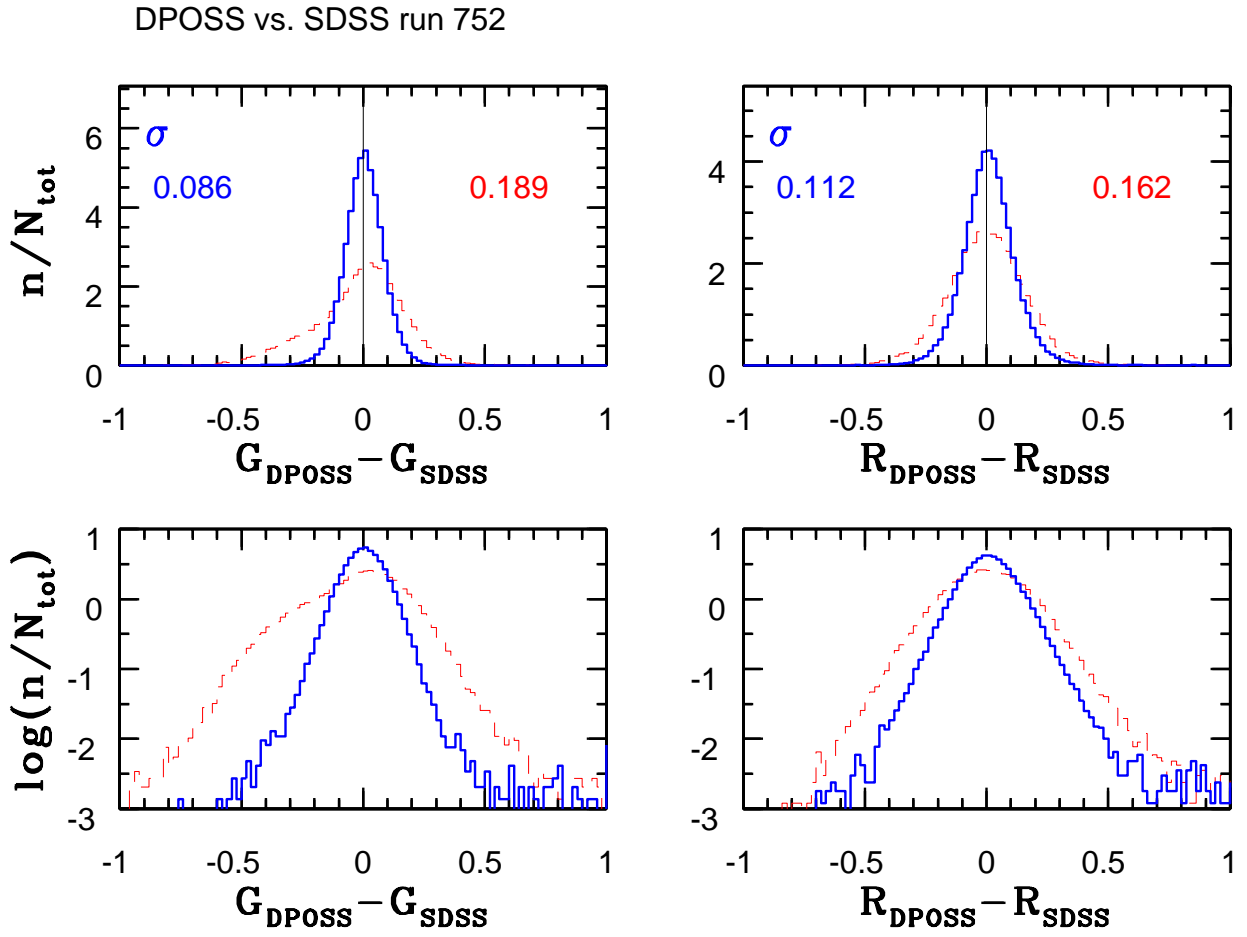


Fig. 12.— Same as Fig. 6, except for the DPOSS catalog.

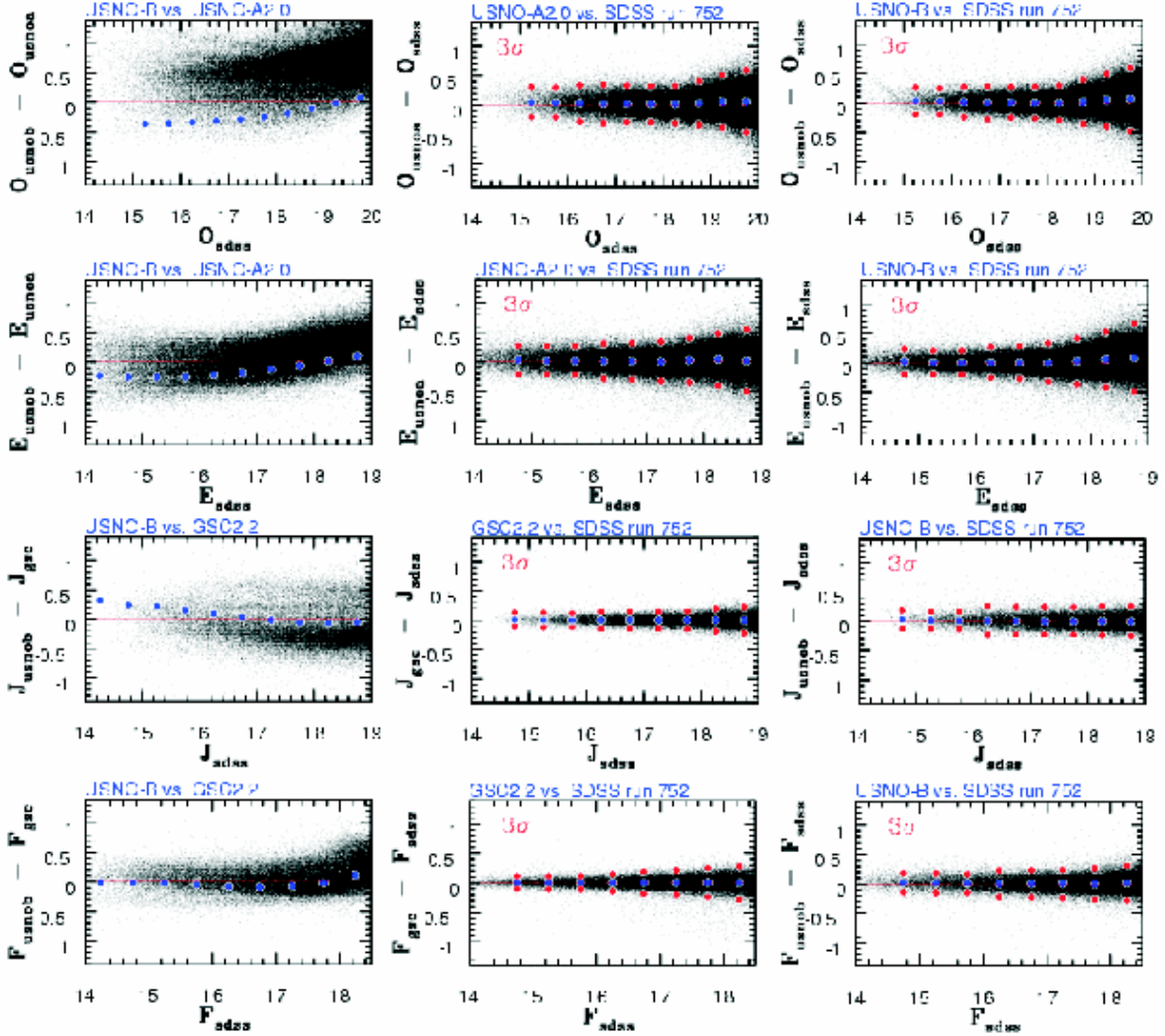


Fig. 13.— A summary of recalibration results for different POSS catalogs, as marked. The POSS-SDSS comparisons, shown in the middle and right columns, are based on the recalibrated magnitudes, while the POSS-POSS comparisons for different input catalogs (left column) are based on their original magnitudes.

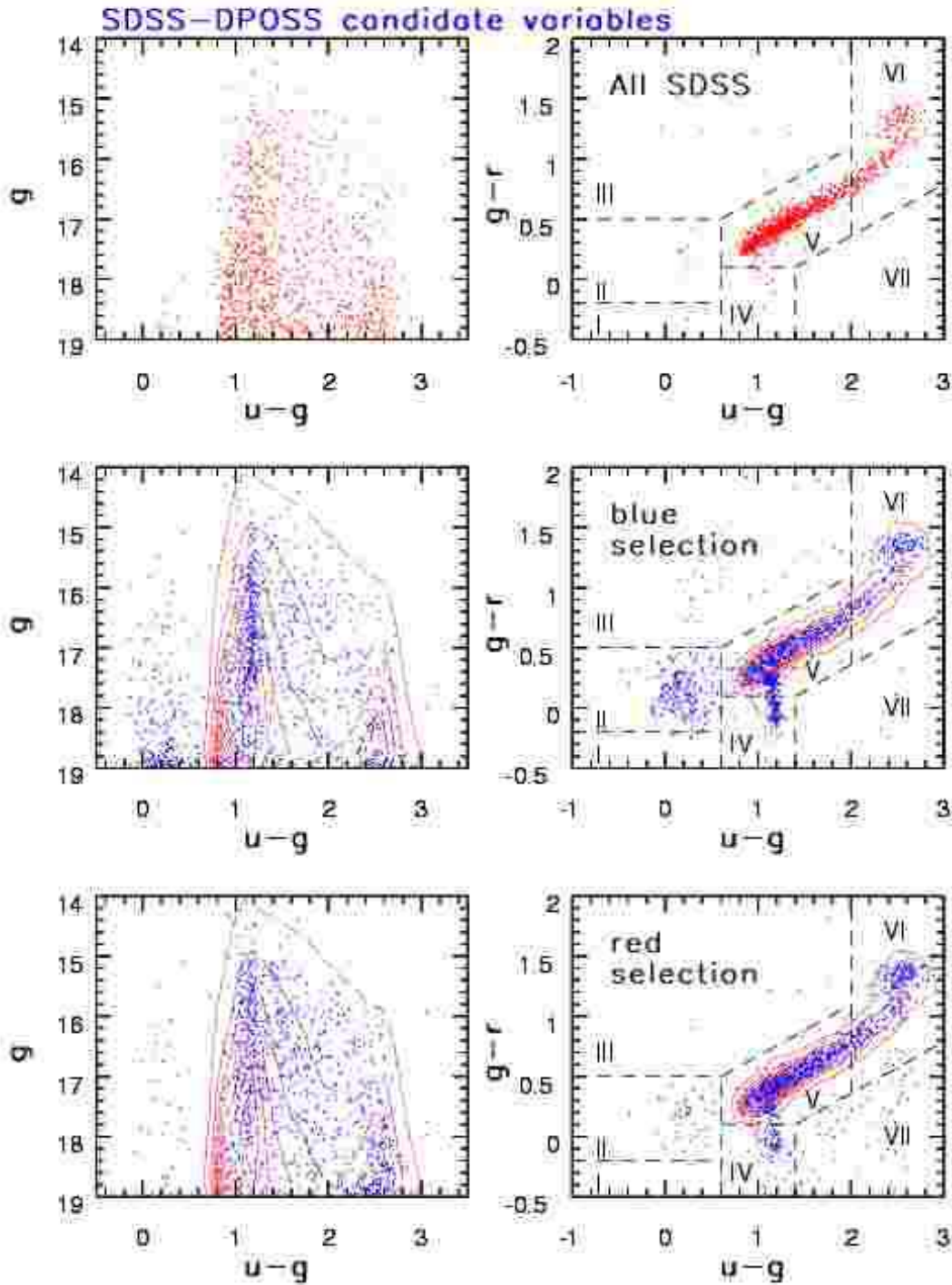
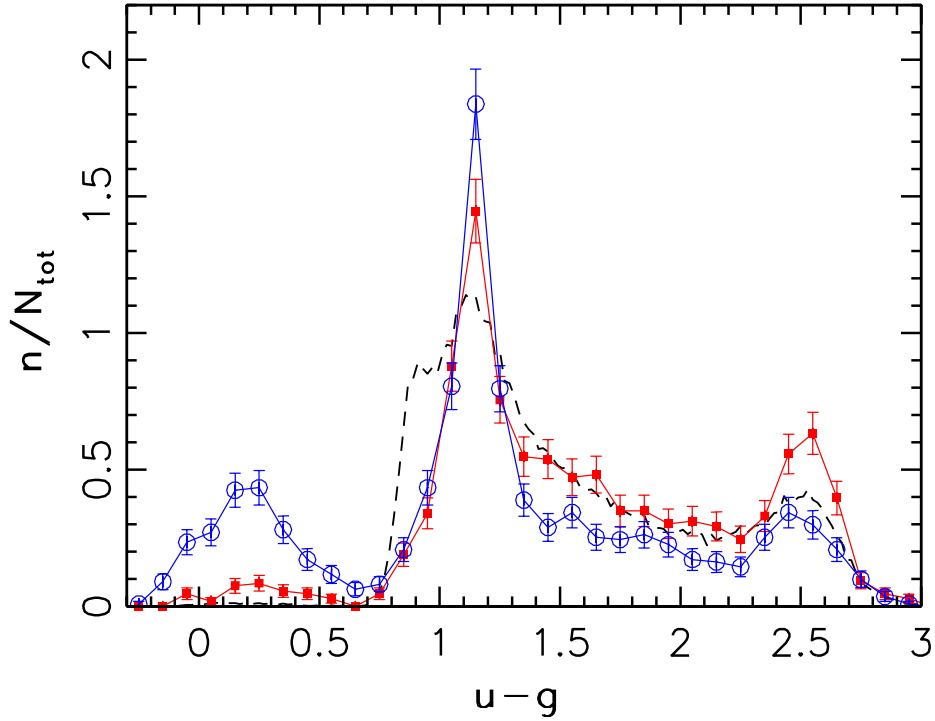


Fig. 14.— The distribution of SDSS-DPOSS candidate variable sources with $g < 19$ in representative SDSS color-magnitude (left) and color-color diagrams (right). The top row is shown for reference and displays a sample of SDSS point sources with the same flux limit and with the same total number of sources (~ 1000). The middle and bottom rows display the distributions from the top row by contours, and variable sources selected from the DPOSS catalog as dots (G selection in the middle row and R selection in the bottom row, see the last two entries in Table 3). The regions marked in the right column are used for quantitative comparison of the overall and variable source distributions (see Table 4).

SDSS-DPOSS candidate variables



SDSS-DPOSS candidate variables, $g-r > 0.4$

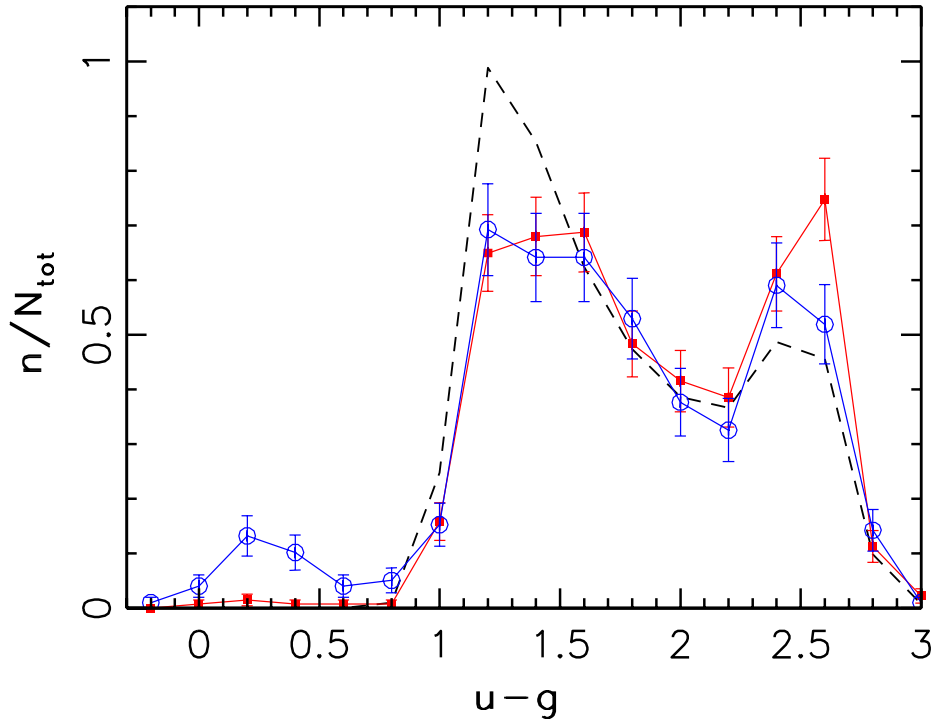


Fig. 15.— The comparison of $u - g$ probability density distributions (i.e. the integrals of the plotted curves are 1 by definition) for SDSS-DPOSS candidate variable sources (symbols with error bars, circles for G selection and squares for R selection), and for a reference sample with the same magnitude limit (dashed line). The top panel shows all sources, and the bottom panel shows a subset with $g - r > 0.4$ (designed to avoid the majority of low-redshift quasars, see Fig. 14). The peak at $u - g \sim 0.2$ is dominated by quasars, the peak at $u - g \sim 1.15$ by RR Lyrae stars, and the peak at $u - g \sim 2.5$ by M stars.

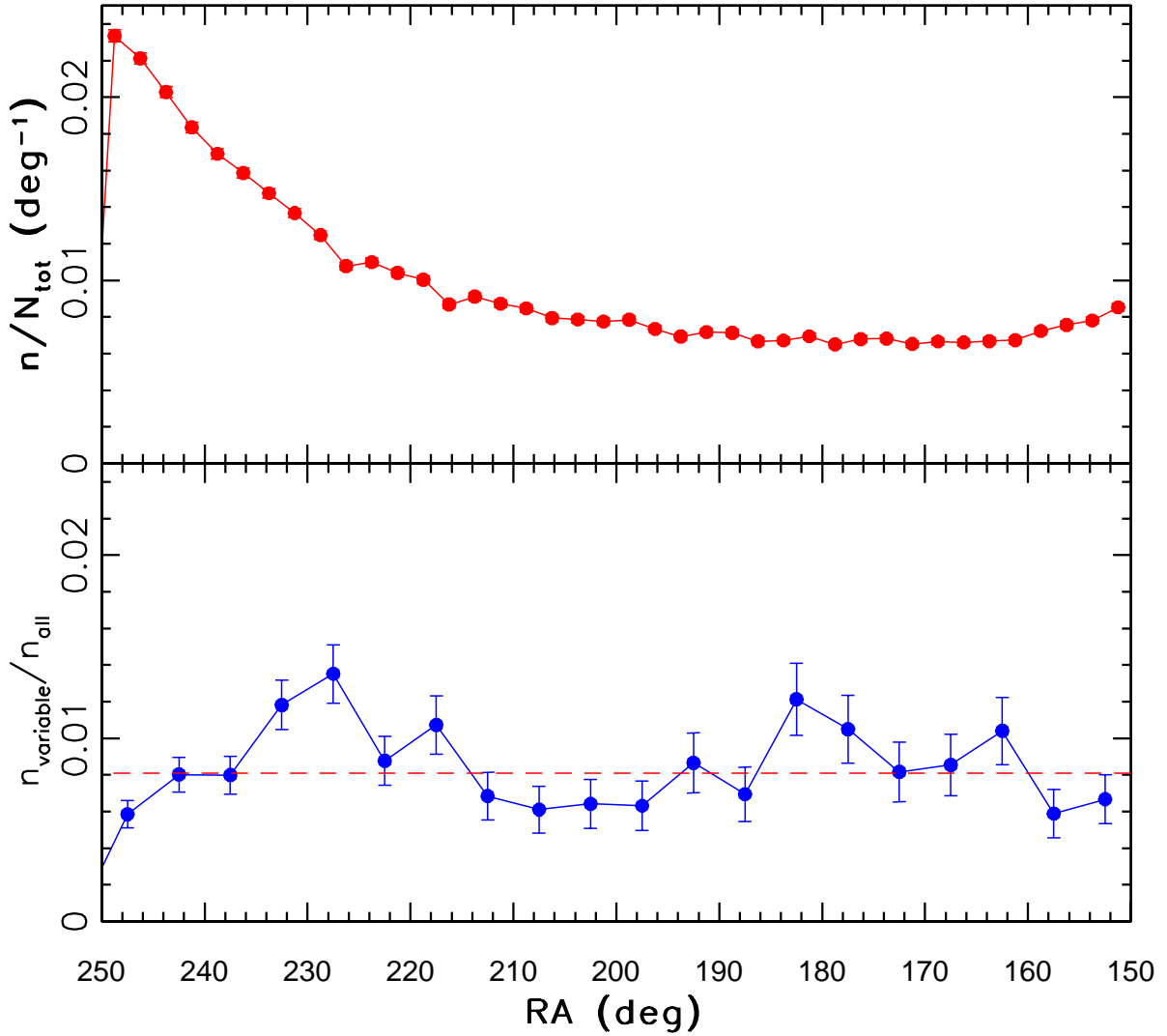


Fig. 16.— The counts of all sources (top) and fraction of candidate variables in a 2.5 deg. wide strip centered on the Celestial Equator, as a function of RA. The counts increase by a factor of ~ 3 towards the left edge because of the decreasing galactic latitude. The fraction of candidate variables stays constant (at 0.8%) within Poissonian noise.

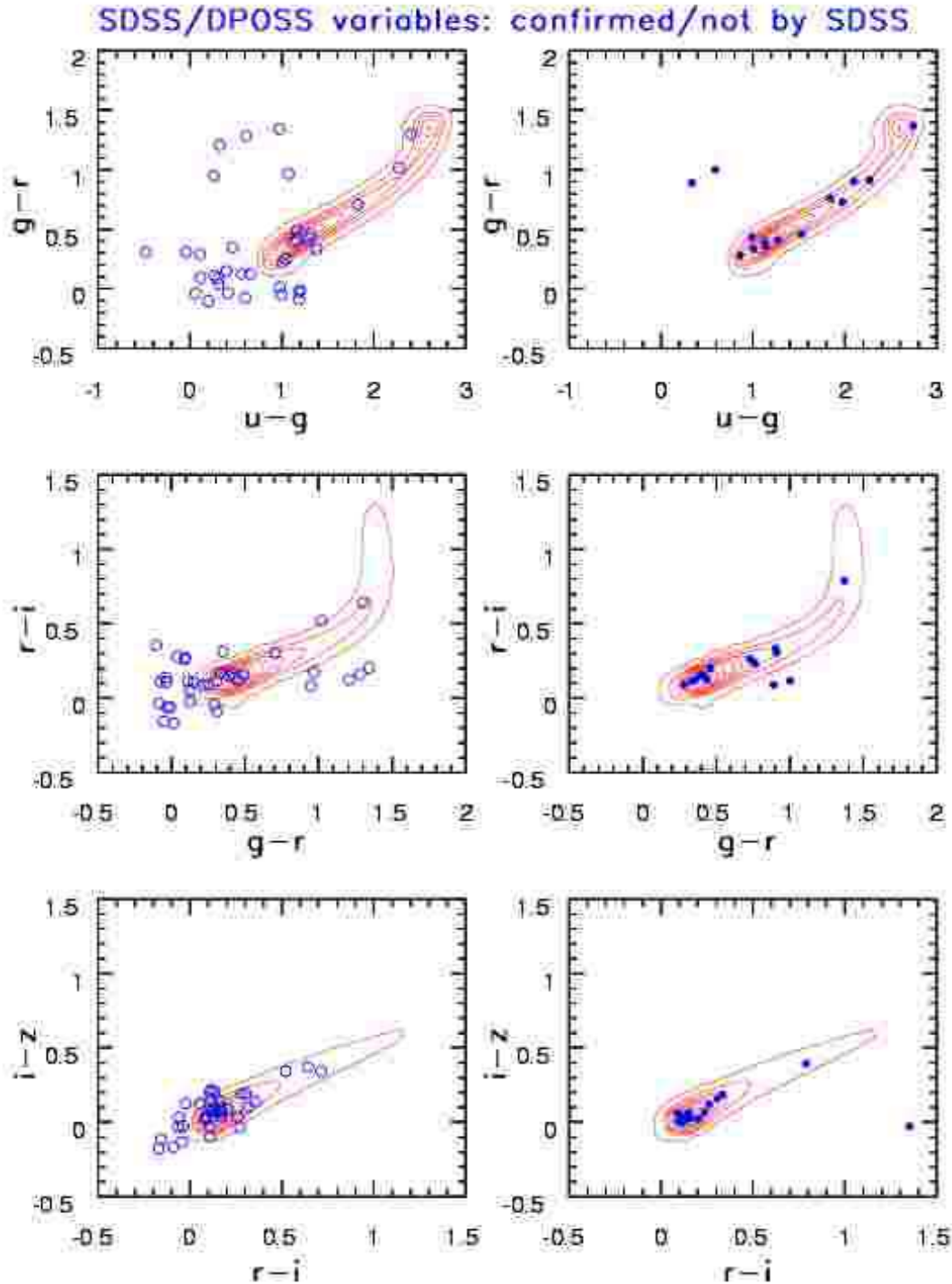


Fig. 17.— The distribution of SDSS-DPOSS candidate variable sources (restricted G selection, see Table 3) confirmed to vary by multi-epoch SDSS imaging (left column, 73% of the sample), and those that did not show any evidence for variability (right column, 27% of the sample). Note that the latter are mostly found in the stellar locus.

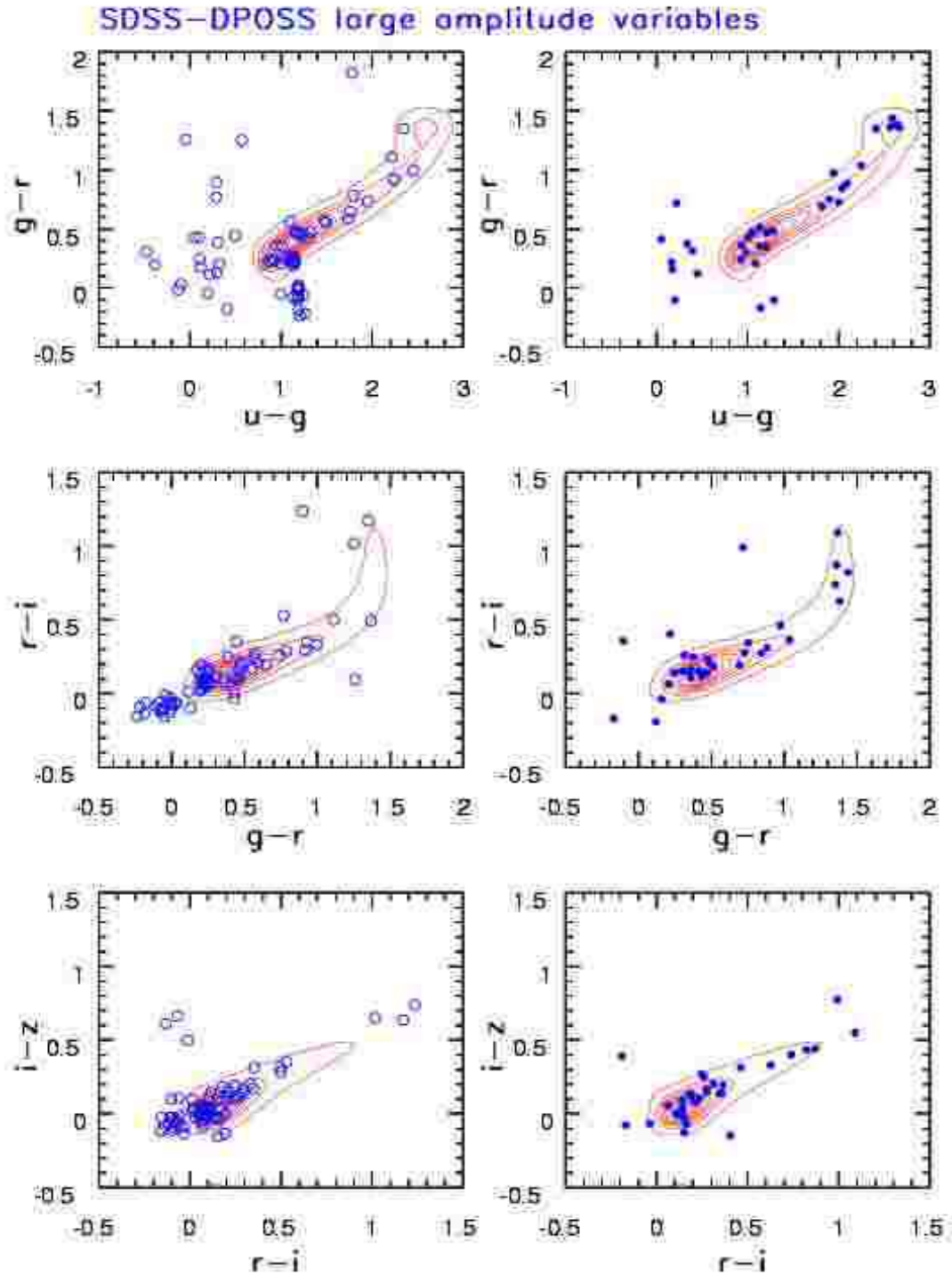


Fig. 18.— The distribution of SDSS-DPOSS candidate variable sources with $14.5 < g < 18.5$ and large amplitudes in representative SDSS color-color diagrams. The symbols show 70 objects with $0.75 < |\Delta G| < 1$ in the left column, and 24 objects with $1 < |\Delta G| < 3$ in the right column. The overall distributions of SDSS sources with the same magnitude limit are shown by contours.

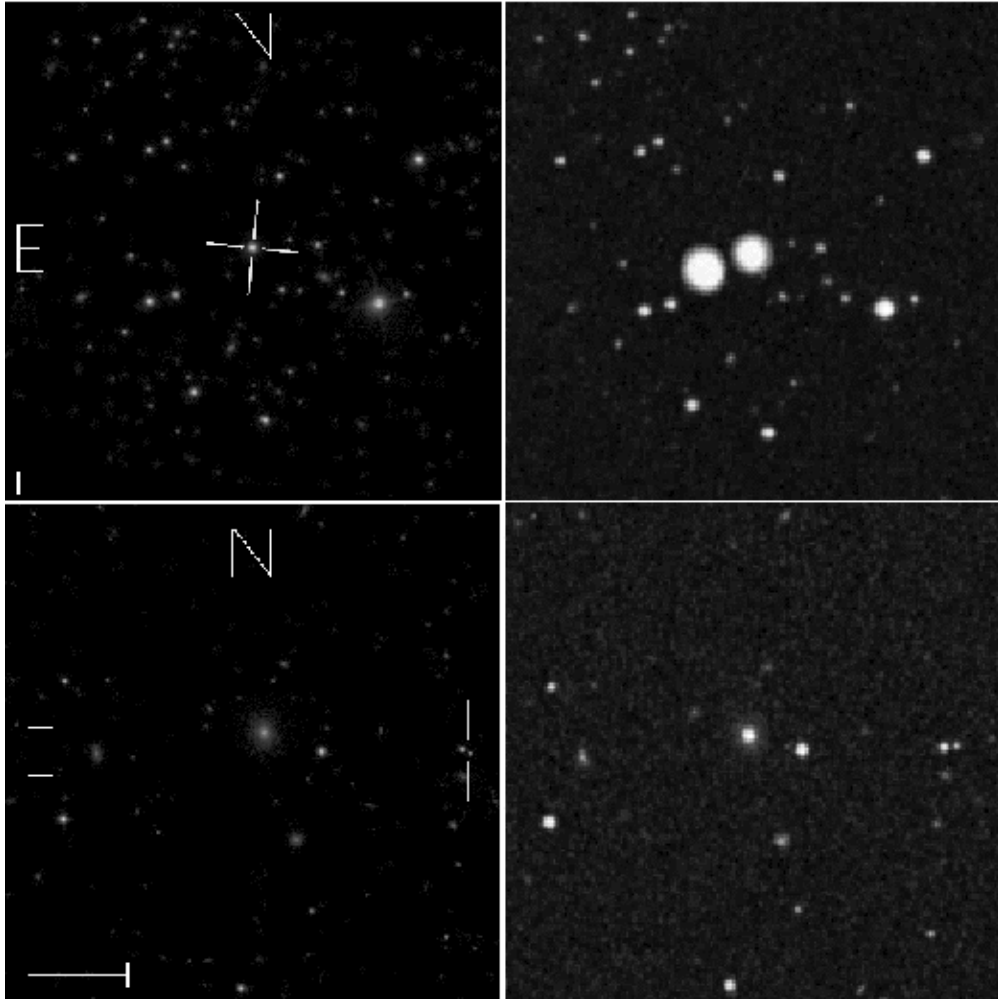


Fig. 19.— Examples of spurious candidate variable sources. The left column displays the 5x5 arcmin g band SDSS images, and the right column displays the blue POSS I images on the same scale, and with the same orientation. In the top panels, the source marked by a cross was selected as a large amplitude candidate variable. The visual inspection of POSS image confirmed that a much brighter source existed in the POSS image, as well as another nearby bright source, both of which turned out to be artefacts. The bottom panels show an example where the POSS photometry was noticeably affected by a nearby source (which happened to be a fast proper motion object).

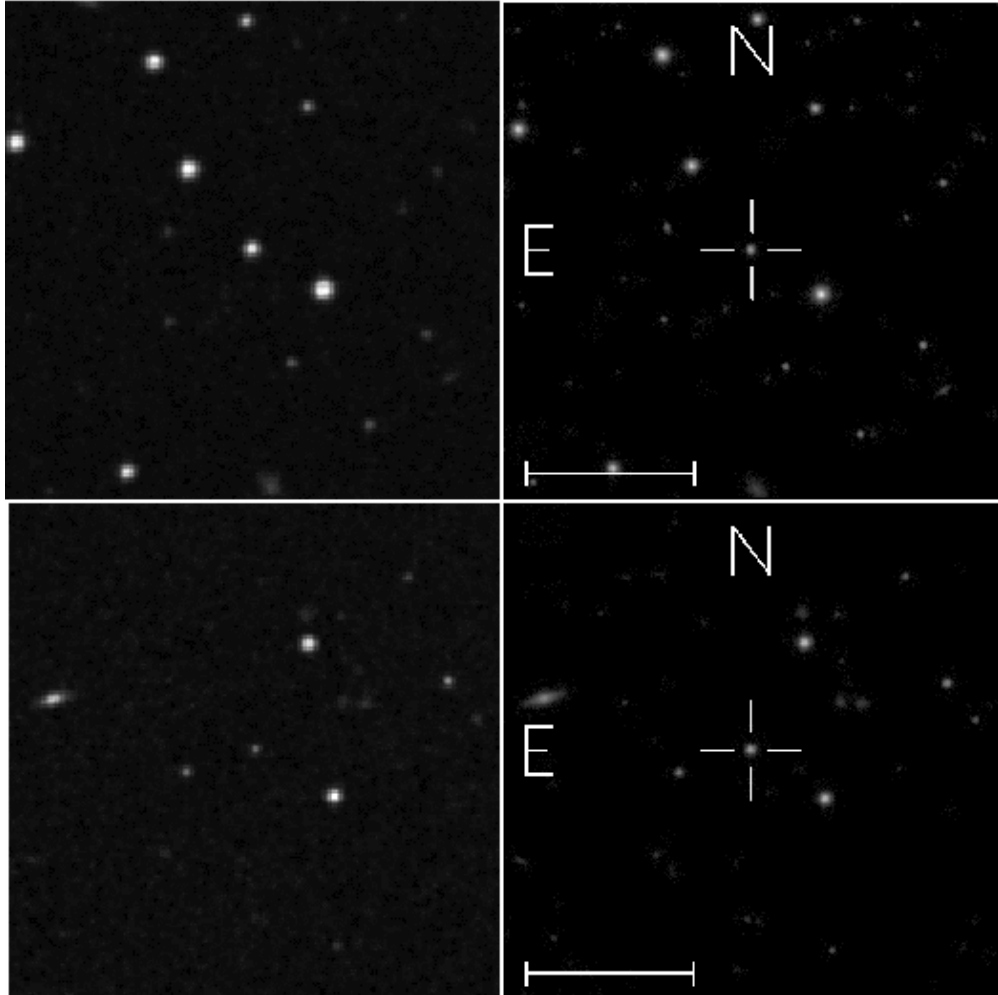


Fig. 20.— Examples of large amplitude (~ 1.5 mag) candidate variable sources. The right column displays the 3×3 arcmin g band SDSS images, and the left column displays the blue POSS II images on the same scale, and with the same orientation. The sources marked by a cross are clearly variable. The top source was brighter in POSS, and the bottom source in SDSS.

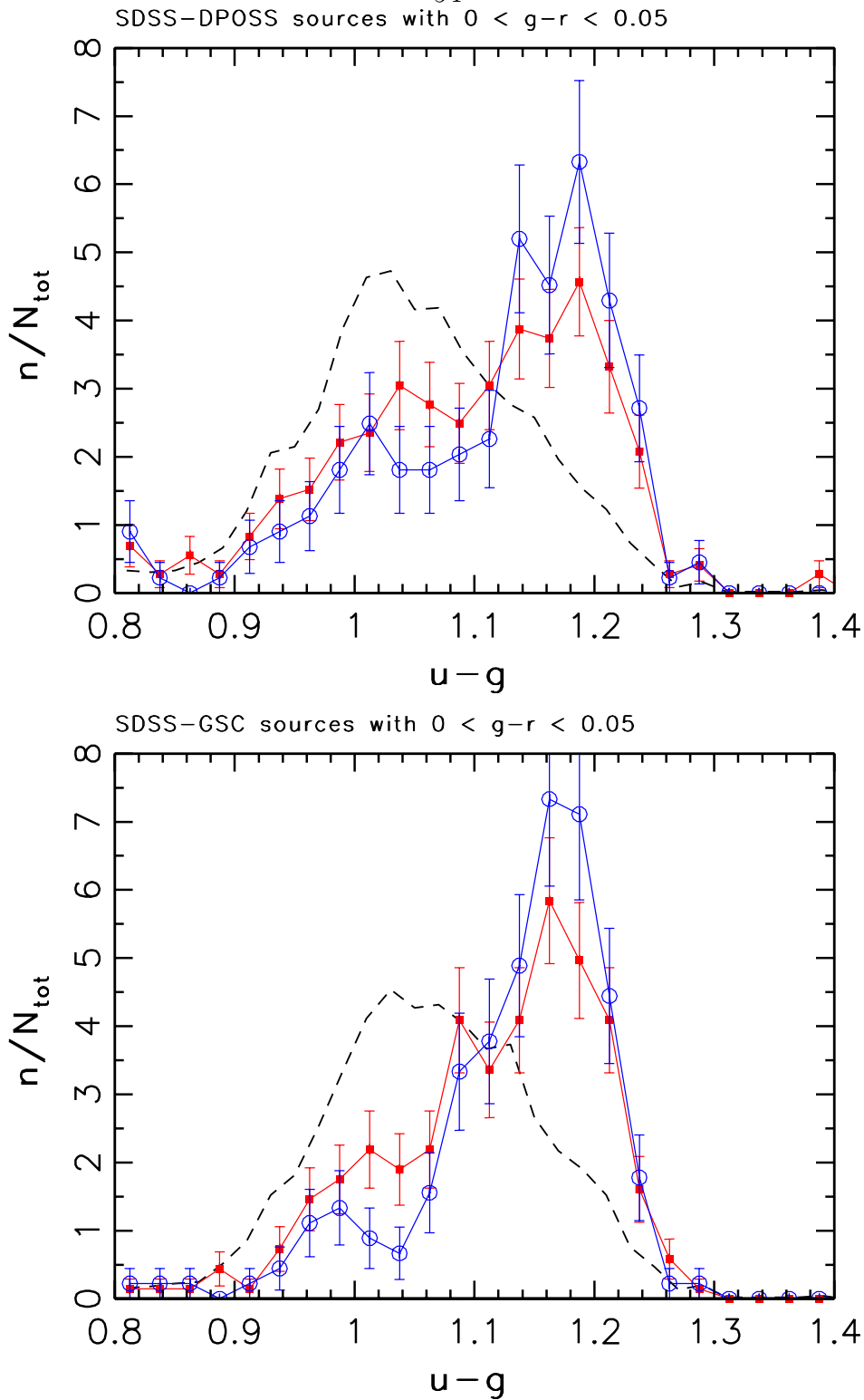


Fig. 21.— The comparison of $u - g$ distributions in the range characteristic for RR Lyrae stars, for candidate variables (symbols with error bars, analogous to Fig. 15), and for a reference sample (dashed line), for sources with $0 < g - r < 0.05$ and $u < 20.5$ (top panel for DPOSS-based selection, bottom panel for GSC; circles for selection in the blue band, squares for the red band). Note that variable objects, dominated by RR Lyrae stars, have redder $u - g$ colors than the reference (full) sample.

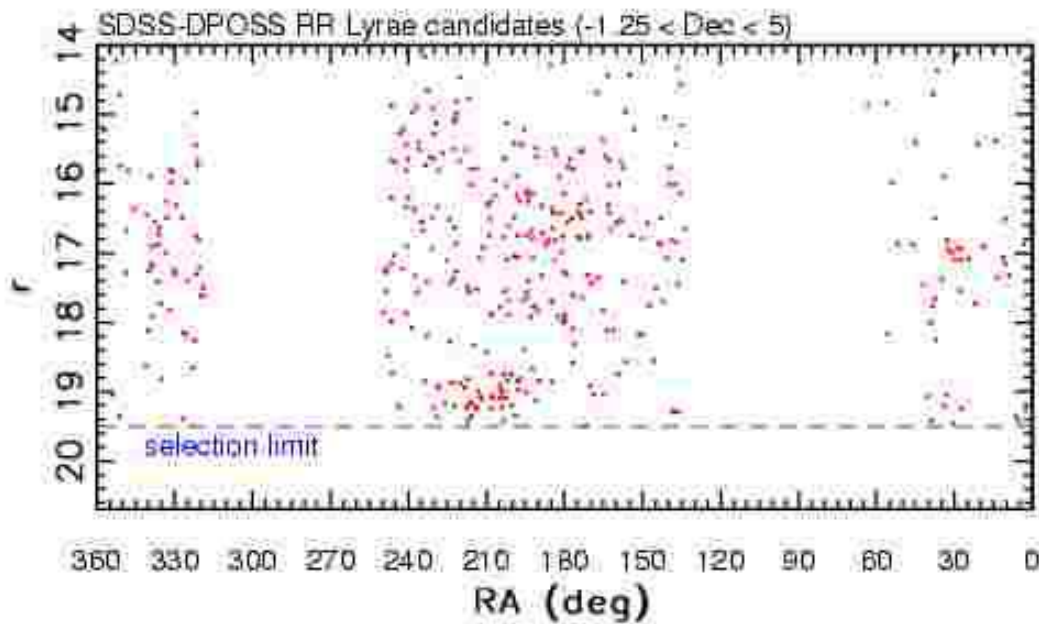


Fig. 22.— The magnitude-position distribution of 350 SDSS-DPOSS RR Lyrae candidates within 5 deg. from the Celestial Equator. The sample completeness is fairly uniform for $r < 19$ and decreases with r towards the selection faint limit of $r = 19.5$. The clumps easily discernible at $(RA, r) \sim (210, 19.2)$ and at $(30, 17)$ are associated with the Sgr dwarf tidal stream. The clumps at $(180, 16.5)$, and at $(330, 17)$ have also been previously reported. The clump at $(\sim 235, \sim 15.5)$ is a new detection.

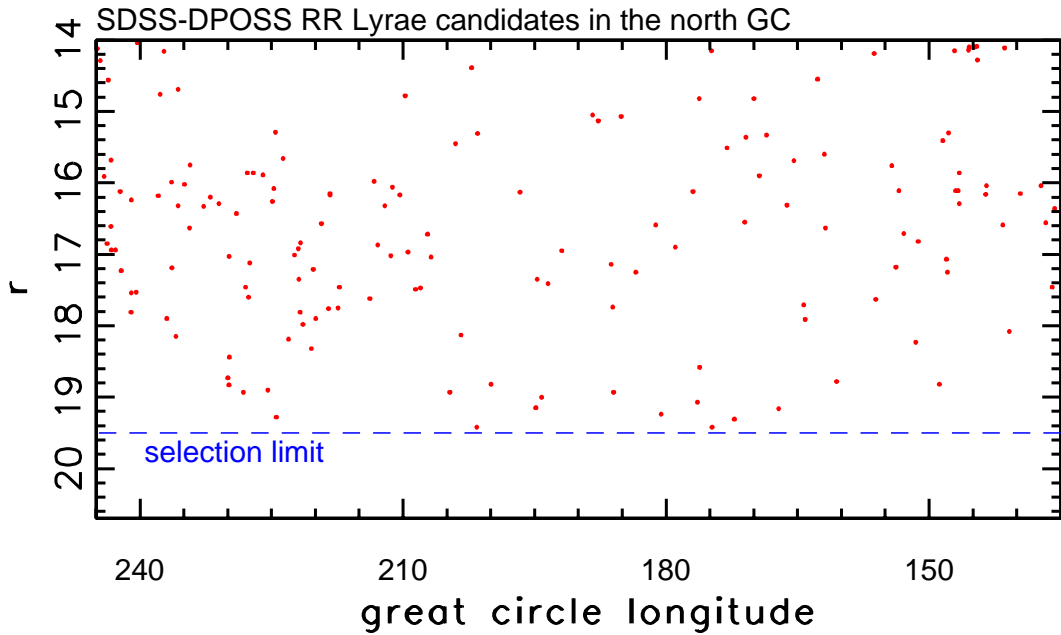


Fig. 23.— Same as Fig. 22, except that the 161 candidates are selected from a 10 deg. wide strip centered on a great circle defined by a node at $RA=95^\circ$ and inclination of 65° (for more details about great circle coordinates see Pier et al. 2003). Note the very inhomogeneous structure, and, in particular, the fairly prominent feature at the longitudes 210-240 ($RA\sim 240^\circ$ and $Dec\sim 50^\circ$), with $r \sim 16-18$.

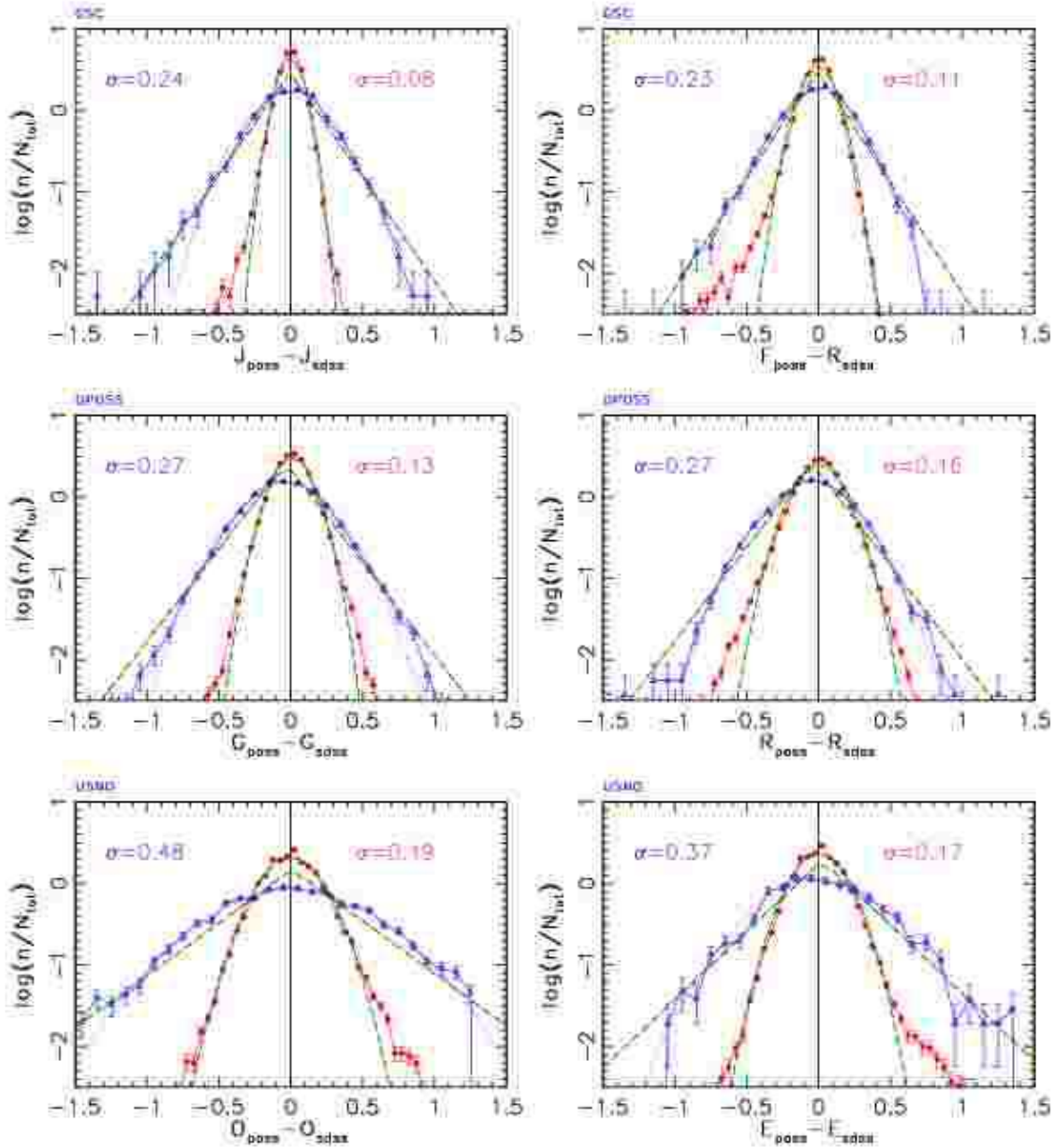


Fig. 24.— The probability density distributions of POSS-SDSS magnitude differences for color-selected low-redshift quasars is shown by triangles, and compared to the corresponding distribution for stars, shown by large dots (note logarithmic scale). The rms for each distribution measured using interquartile range is also shown in each panel. The solid lines show Gaussian distributions that have the same rms scatter as the data. Note that magnitude differences for stars are well described by a Gaussian. The dot-dashed lines show an exponential distribution that has the same rms as the data for quasars, and seem to provide a marginally better fit than a Gaussian distribution.

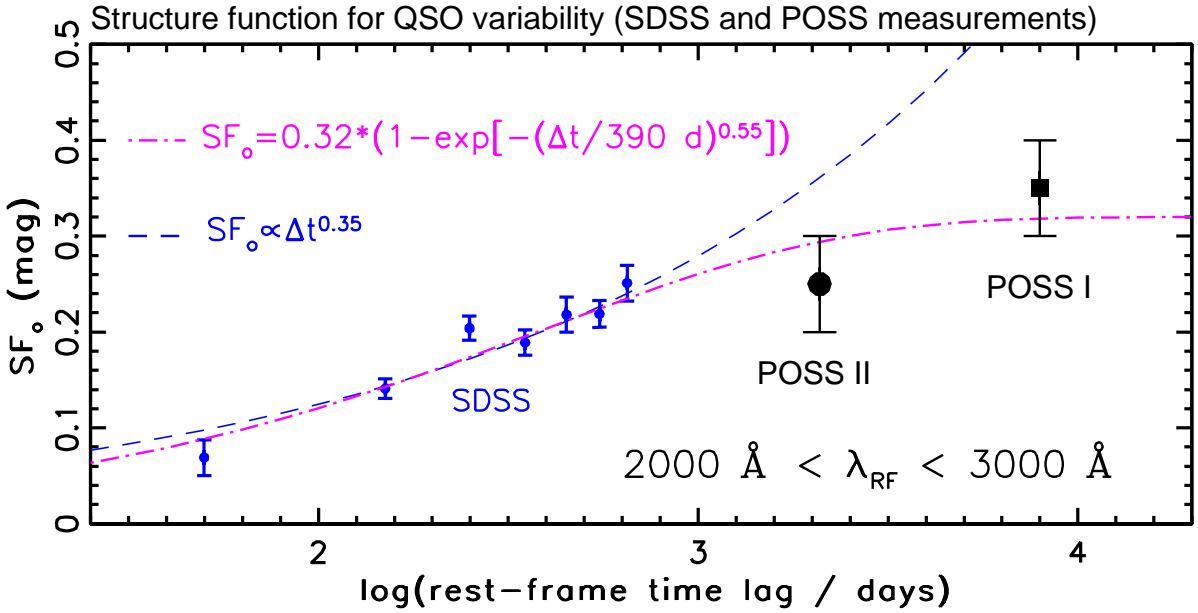


Fig. 25.— The long-term dependence of structure function on rest-frame time lag, in the range 2000–3000 Å, for two data sets: SDSS-SDSS for short time lags (small symbols, adopted from I04), and SDSS-POSS for long time lags (large symbols). The observed SDSS-POSS long-term variability is smaller than predicted by the extrapolation of the power-law measured for short time scales using repeated SDSS imaging (dashed line): the measured values are 0.35 and 0.24 mag, while the extrapolated values are 0.60 and 0.35 mag for SDSS-POSS I and SDSS-POSS II, respectively. The dot-dashed line shows a simultaneous best-fit to all the displayed data.

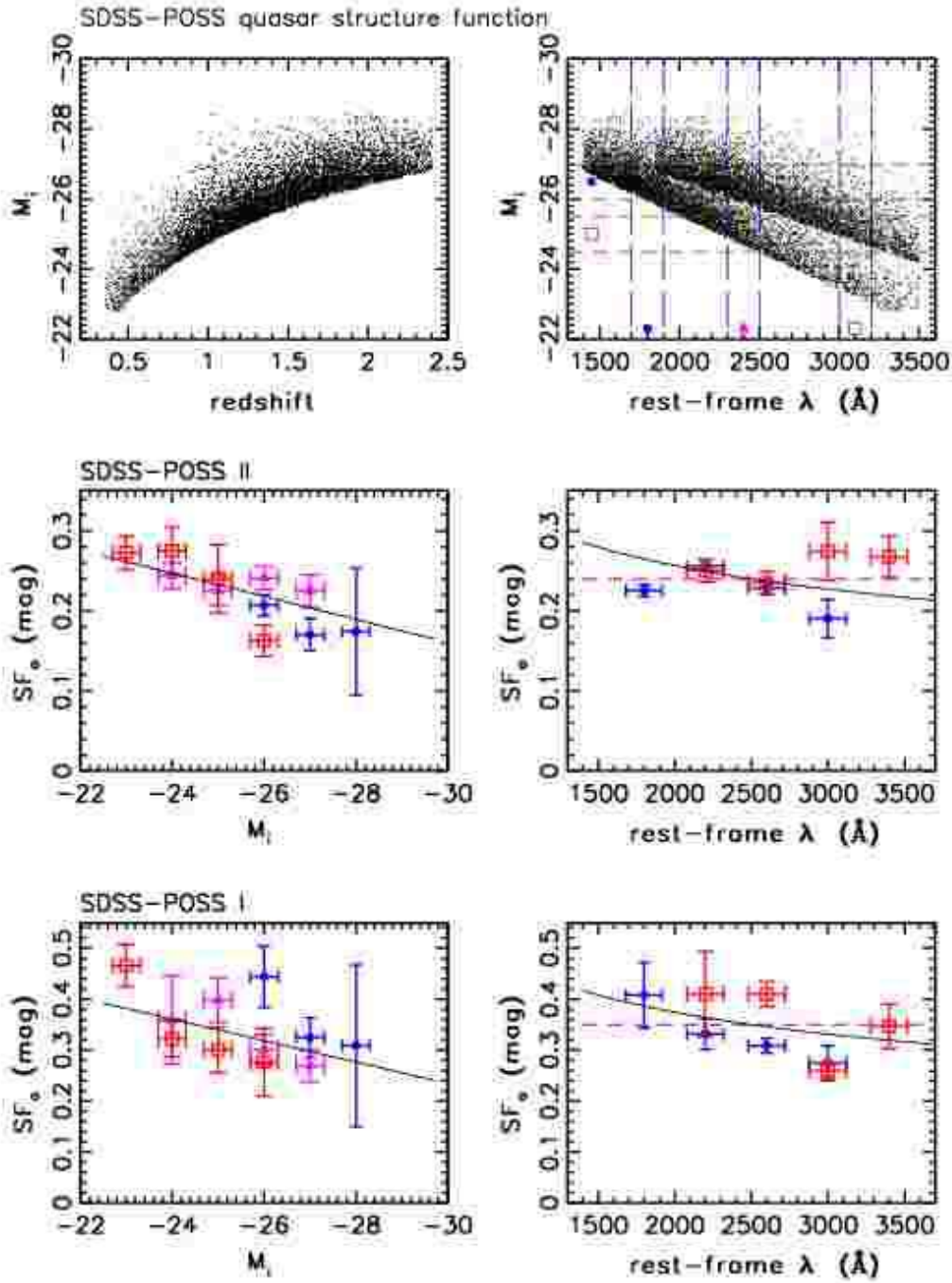


Fig. 26.— The top two panels show the distribution of 7,279 quasars with $i < 19$, $G_{SDSS} < 19$, and redshifts in the range 0.3–2.4, in the redshift vs. M_i (left) and M_i vs. rest-frame wavelength (right) planes. The remaining four panels show structure function as a function of M_i and rest-frame wavelength for objects selected in narrow bins marked in the top right panel (the symbols in each strip are used to mark the corresponding histograms). The middle two panels correspond to SDSS-POSS II comparison, and the bottom two panels to SDSS-POSS I comparison. The solid lines in the two left panels show the correlation $SF \propto 1 + 0.024 M_i$, inferred by I04 from repeated SDSS imaging scans. The dashed lines in the two right panels represent median values, and the solid lines are the relationship $SF \propto \lambda^{-0.3}$, derived from repeated SDSS imaging data. See text for discussion.